

**A MINIMUM-BENDING-ENERGY NEEDLE MODEL
FOR CLOSED-LOOP LOCALIZATION DURING
IMAGE-GUIDED INSERTION**

by

Joseph Schornak

A Thesis submitted to the Faculty of the

WORCESTER POLYTECHNIC INSTITUTE

in partial fulfillment of the requirements for the

Degree of Master of Science in Biomedical Engineering

Worcester, Massachusetts

May, 2018

© Joseph Schornak 2018

All rights reserved

Approved by:

Prof. Gregory S. Fischer, Advisor
Worcester Polytechnic Institute

Prof. Jie Fu, Committee Member
Worcester Polytechnic Institute

Prof. Loris Fichera, Committee Member
Worcester Polytechnic Institute

Abstract

Accurate needle placement is critical to the success of needle-based interventions. Needle deflection due to tissue non-homogeneity and dynamic forces results in targeting error, potentially requiring repeated insertions. Real-time imaging enables closed-loop control of the needle during insertion, improving insertion accuracy. The needle localization algorithm proposed in this thesis models the needle as a parametric polynomial equation optimized to minimize beam bending energy relative to a set of observed needle coordinates. Simulated insertions using an MRI dataset show that the minimum bending energy model allows planning of subsequent imaging planes to capture the moving needle while estimating the shape of the needle with low error.

Contents

Abstract	iii
List of Figures	vii
1 Introduction	1
1.1 Motivation	1
1.2 Problem Formulation	3
1.3 Thesis Contributions	4
1.3.1 Needle Modeling by Minimization of Bending Energy	4
1.3.2 Imaging-Agnostic Needle Tip Localization Algorithm	4
1.3.3 MRI Data Collection	5
1.3.4 Slicer Module	5
1.4 MRI Physics	6
1.5 Tissue Phantoms	7
2 Review of Previous Work	10
2.1 Needle Geometry	10

2.2	Needle Modeling	11
2.2.1	Non-Holonomic Kinematics	12
2.2.2	Finite Element Models	13
2.2.3	Mechanical Models	14
2.3	Needle Steering	15
2.4	Needle Localization	18
2.4.1	Coronal and Sagittal Plane Imaging	19
2.4.2	Transverse Plane Imaging	21
2.4.3	3D Imaging	22
2.4.4	Non-Imaging Techniques	23
3	Needle Model	25
3.1	Assumptions	27
3.2	Beam Bending Energy	29
3.3	Parametric Polynomial Space Curves	30
3.4	Curve Fitting	31
3.4.1	Cost Function	32
3.4.2	Constraints	33
3.4.3	Assumptions	34
3.5	Software Implementation	34
4	Needle Localization in MR Images	38

4.1	Software Architecture	38
4.1.1	Simulated MRI Scanner	38
4.1.2	Needle Tracking Module	39
4.2	Experiment	40
4.2.1	MRI Data Collection	41
4.2.2	Needle Localization	41
4.3	Results	42
4.3.1	Needle Localization at a Single Timestep	43
4.3.2	Needle Localization at Sequential Timesteps	44
5	Discussion and Conclusion	52
5.1	Discussion	52
5.1.1	MRI Experiment	52
5.1.2	Needle Model	53
5.2	Future Work	54
5.3	Conclusion	55
References		56

List of Figures

1.1	A manual MRI-guided biopsy in progress (from Tokuda, 2012 [1]).	2
1.2	MRI scan of a pelvic region undergoing biopsy.	7
1.3	MRI scan of a gelatin tissue phantom undergoing needle insertion. The needle enters the phantom at the right of the image. Note the artifact around the needle tip.	8
1.4	Gelatin tissue phantom similar to the ones used in this thesis.	9
2.1	Free-body diagram depicting forces acting on the needle tip during insertion into an elastic medium (from Misra, 2010 [2]).	11
2.2	Point and distributed forces acting on the needle during insertion (from Roesthuis, 2012 [3]).	12
2.3	Nonholonomic model in which the needle tip is represented as a bicycle with a fixed front-wheel steering angle (from Webster, 2006 [4]).	13
2.4	Finite element model which represents the needle as a series of angular springs interacting with a 2D mesh [5].	14
2.5	Mechanical model of a needle in a two-bend configuration (from Roesthuis, 2012 [3]).	16
2.6	Example of a needle with a pre-curved tip [6].	18
2.7	Custom-manufactured steerable needle with an actuated tip and Fiber Bragg Grating strain gauges (from Roesthuis, 2015 [7]).	19
2.8	Example of a steerable concentric-tube needle (from Rucker, 2010 [8]).	20
2.9	Alternating-planes strategy to track the needle tip during insertion (from Patel, 2015 [9]).	21
2.10	Needle tracking in US via imaging in the transverse plane (from Vrooijink, 2014 [10]).	22
2.11	Catheters semi-automatically segmented in 3D MRI data using the NeedleFinder Slicer extension (from Pernelle, 2013 [11]).	23
2.12	Placement of Fiber Bragg Grating sensors on a specially-modified needle (from Roesthuis, 2014 [12]).	24

3.1	Given a number of samples, the spacing between the samples, an offset distance from the needle tip, and a new needle base pose, the expected coordinate of the needle is calculated at each sample point.	35
3.2	New imaging is collected at each needle coordinate, and the actual position of the needle is observed.	36
3.3	A new polynomial curve is calculated, optimized to minimize both the cumulative bending energy in the needle and the error between the curve and the observed points.	37
4.1	System architecture for needle detection and modeling from MRI data.	39
4.2	User interface for MRINeedleTipTracker 3D Slicer module.	40
4.3	Tissue phantom with needle alignment frame and biopsy needle. . . .	42
4.4	Segmentation of needle artifact generated by thresholding MRI volume.	43
4.5	Baseline ground truth data, calculated from the centroids of the segmented artifact sectioned in the X-Y plane.	44
4.6	Magnitude of in-plane error over insertion for various degrees of polynomial. Markers indicate the positions of the slices on the needle curve. $d = 26.0\text{mm}$, $k = 3$, $\delta = 5.0\text{mm}$	45
4.7	Magnitude of in-plane error over insertion for a variable number of sample points. $n = 5$, $\delta = 5.0\text{mm}$	46
4.8	Example polynomial curve fit plotted against the positions of the artifact centroids in transverse plane.	47
4.9	Positions of 2D scan planes at each insertion step, with segmented artifact.	48
4.10	Modeled curve points at each insertion step, with segmented artifact.	49
4.11	Magnitude of error between the needle model and the artifact centroid. $d = 10\text{mm}$, $k = 3$, $\delta = 5\text{mm}$	50
4.12	Magnitude of error between the needle model and the artifact centroid, where the spacing between each slice increases with insertion depth. $d = 10\text{mm} + \text{index}_{\text{step}} * 4\text{mm}$, $k = 3$, $\delta = 5\text{mm}$	51

Chapter 1

Introduction

1.1 Motivation

Many interventional procedures rely on needle insertion, including biopsy and brachytherapy [13]. Accurate needle placement is a critical factor in the success of these procedures [14, 15]. Deflection of the needle tip during insertion and variation in the mechanical properties of tissue can cause the needle to deviate from its expected trajectory and miss the target. This can be mitigated by using an alignment structure to aim the needle at the target and verifying that the correct position has been reached in post-operative imaging [1]. Even with preoperative image-based planning and careful alignment with the target, several insertions may be required to attain the desired needle placement [16].

Live intra-operative imaging of the needle throughout insertion reduces error

caused by needle deflection by allowing the surgeon to see if the needle is deviating from its trajectory and take corrective action. Ultrasound (US) and Magnetic Resonance Imaging (MRI) are preferred imaging modalities. While US is portable and hand-steerable, MRI offers superior resolution of soft tissues compared to both US and CT [17]. Manually-controlled image-guided needle insertion is still a challenging task. Under MRI guidance the confined space of the scanner bore, illustrated in Figure 1.1, limits the surgeon's visibility and range of motion [?, 18].

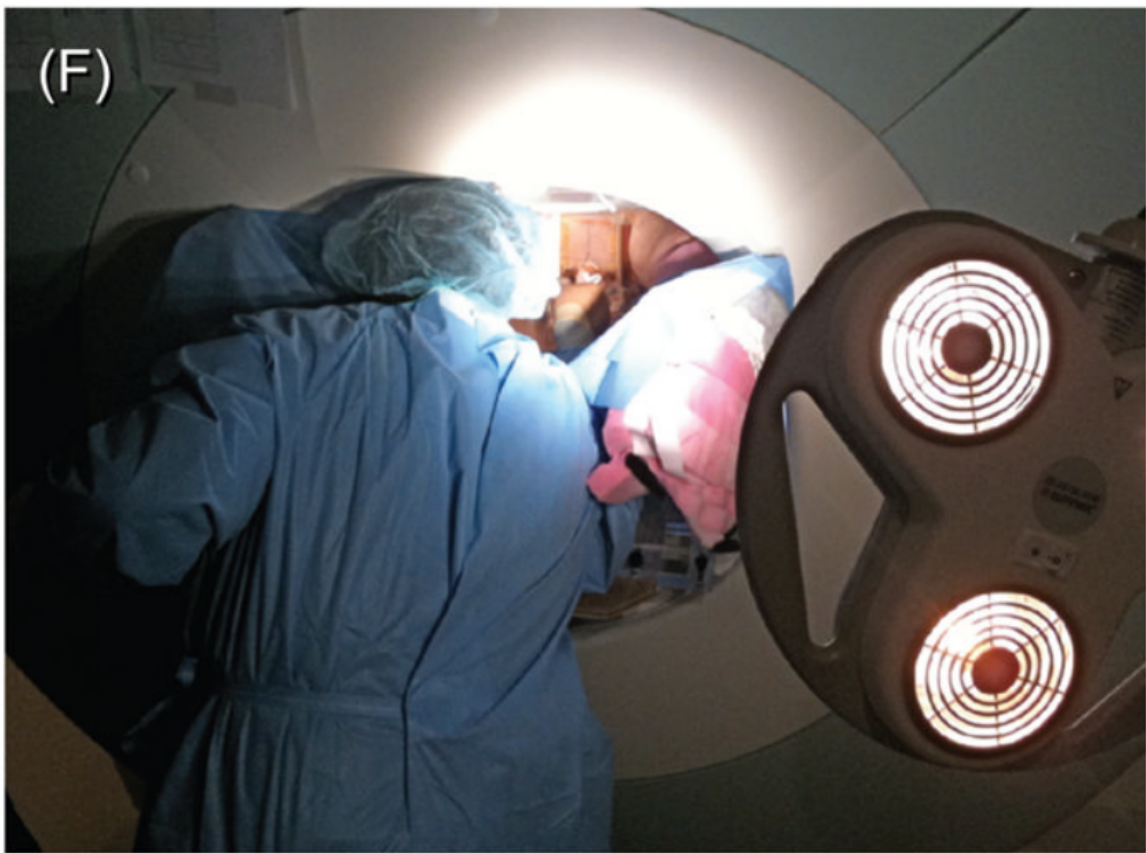


Figure 1.1: A manual MRI-guided biopsy in progress (from Tokuda, 2012 [1]).

Robotically-controlled needle insertion solves some of the challenges of live intra-

operative MRI imaging by reducing the clinician’s workload and moving them out of the scanner bore. (CITE!)

Using live imaging, an insertion robot can correct for unmodeled tip deflection and keep the needle on its expected trajectory, improving the success rates of biopsies and other needle-based interventions. (CITE!)

Several collaborative needle insertion robots have been demonstrated. These allow the surgeon to control the rate of needle insertion while the robot controls the orientation of the needle. (CITE!)

Previous work has shown that closed-loop control of MRI [9] and US [10] coupled with image processing techniques for needle localization can track a needle tip during insertion with a useful degree of accuracy.

1.2 Problem Formulation

A key requirement in closed-loop image-guided needle insertion is the accurate measurement of the 6-degree-of-freedom pose of the needle tip using data from the imaging system. Accurate tip localization is required for the needle controller to determine the correct control input which minimizes the error between the current needle tip pose and the desired trajectory. Searching for the needle in each image on an individual basis introduces errors due to imaging artifacts, noise, and structures near the needle, contributing to reduced tip localization accuracy. A needle model that

combines data from real-time imaging with the kinematics of the insertion platform and the mechanical properties of the needle would allow accurate estimation of the pose of the needle tip while requiring comparatively few observations of the needle position.

1.3 Thesis Contributions

1.3.1 Needle Modeling by Minimization of Bending Energy

This thesis presents an approach to needle modeling that uses the mechanical bending properties of the needle, the pose of the needle base, and a set of observed needle positions along the needle shaft to find a configuration of the needle that minimizes its bending energy while meeting the observed constraints. In this model is represented by a three-dimensional parametric polynomial curve.

1.3.2 Imaging-Agnostic Needle Tip Localization Algorithm

The needle model provides continuous needle pose estimates along its shaft, which can be used to plan imaging to observe the needle position after motion. The expected

position of the needle informs the search for the actual position of the needle in received images, which reduces localization error caused by noise and other shapes near the needle. Since the needle model is updated using a set of positions along the needle shaft instead of the position of the needle tip, updates can be performed using imaging in planes transverse to the needle rather than imaging in the coronal and sagittal planes. This mitigates the risk of loss of needle tracking during insertion.

1.3.3 MRI Data Collection

MRI scans were collected depicting a biopsy needle being inserted into a gelatin tissue phantom. An alignment structure restricted the pose of the needle base during insertion, allowing each scan at a regular insertion interval to be associated with a needle pose.

1.3.4 Slicer Module

An extension for 3D Slicer, an open-source medical imaging program [19, 20], was created to evaluate the needle model when applied to the MRI dataset. The user interacts with the needle model through the Needle Tracking module, which accepts inputs for the current needle base pose and the current 3D scan in the MRI dataset and returns polynomial coefficients representing the current state of the needle. A supporting MRI Reslicer module converts the 3D MRI scans into 2D slices at specified

depths, which simulates part of the functionality of an MRI machine.

1.4 MRI Physics

Magnetic Resonance Imaging (MRI) is used to image material containing hydrogen ions, or protons, such as human tissue. The strong magnetic field of the MRI machine causes the free protons to align along the axis of the field. A pulse of radiofrequency (RF) radiation excites the protons, which subsequently emit RF energy as they return to a lower-energy state. The emitted energy is measured by the scanner to generate and image of the tissue based on the intensity of the return from different areas.

Performing an MRI scan on a material that does not contain any free protons, such as plastic or metal, produces a dark void in the image. Metal objects distort the magnetic field, producing susceptibility artifacts around the objects. The shape and extent of the artifact depends on the parameters of the MRI scan sequence, the shape of the object, and the material. Needles and wires behave like antennae in the MRI environment, so they produce imaging artifacts around their tips [21]. Determining the position of the needle using its imaging artifact is the basis for needle tracking in MRI [22].



PLACEHOLDER

Figure 1.2: MRI scan of a pelvic region undergoing biopsy.

1.5 Tissue Phantoms

Synthetic tissue phantoms are often used during needle insertion studies instead of ex-vivo tissue specimens. These phantoms are designed so their mechanical properties reflect those of human tissue. They offer several benefits over real tissue, especially in the context of benchtop laboratory experiments.

1. Phantoms made of gelatin or plastic are transparent, so vision-based methods can be used for needle tracking or for validation of other imaging modalities.

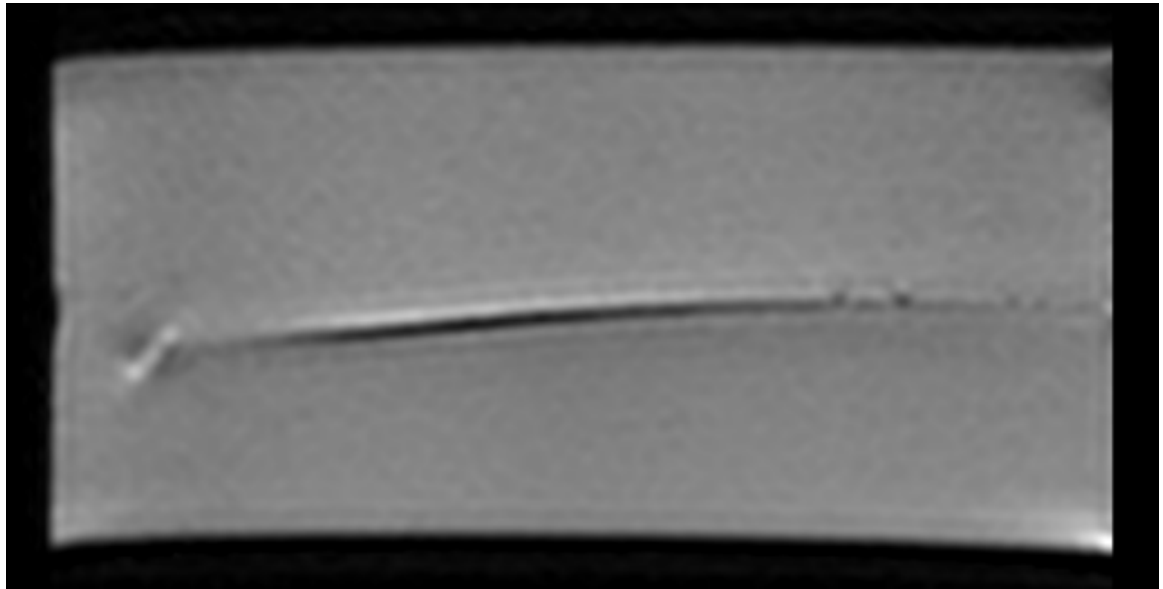


Figure 1.3: MRI scan of a gelatin tissue phantom undergoing needle insertion. The needle enters the phantom at the right of the image. Note the artifact around the needle tip.

2. A needle inserted into a homogeneous tissue phantom will experience constant cutting force throughout insertion.
3. Phantoms can include multiple regions with different mechanical properties separated by membranes.
4. Phantoms have a much longer shelf life than tissue, granting more flexibility to studies.



PLACEHOLDER

Figure 1.4: Gelatin tissue phantom similar to the ones used in this thesis.

Chapter 2

Review of Previous Work

2.1 Needle Geometry

Beveled-tip needles deflect during insertion due to asymmetric cutting force at the needle tip. The cutting forces on the tip of the needle, shown in Figure 2.1 can be modeled as a point load with transverse and radial components relative to the needle shaft [2]. Friction and damping force are transverse forces distributed along the needle shaft, while pushback from deformed tissue is a distributed radial force. Figure 2.2 shows the point and distributed loads on the needle shaft.

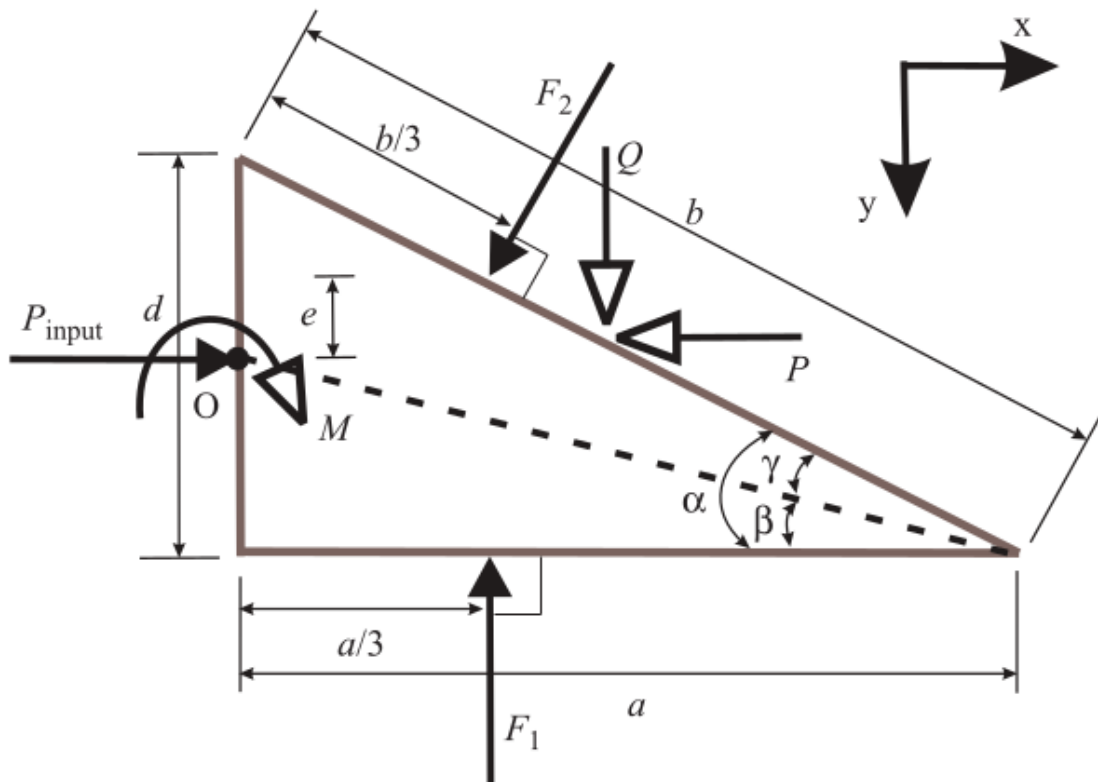


Figure 2.1: Free-body diagram depicting forces acting on the needle tip during insertion into an elastic medium (from Misra, 2010 [2]).

2.2 Needle Modeling

The goal of research in this area is to produce a model of needle behavior that accurately predicts the motion of the needle tip during insertion so that a needle trajectory can be planned and accurately followed even when few or no needle tip observations can be made.

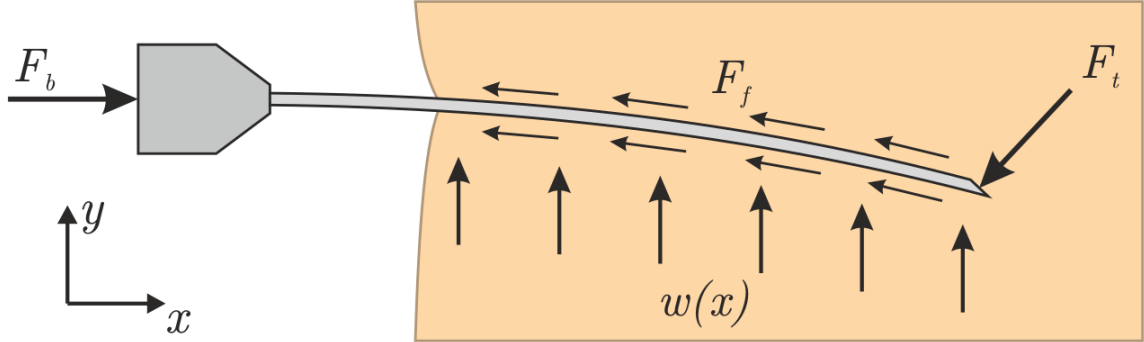


Figure 2.2: Point and distributed forces acting on the needle during insertion (from Roesthuis, 2012 [3]).

2.2.1 Non-Holonomic Kinematics

The non-holonomic kinematics of a beveled-tip needle can be represented by modeling the needle as a bicycle with the front wheel fixed at a constant steering angle [4, 23]. This model is illustrated in figure 2.3. Since the steering angle is determined by the shape of the needle, the stiffness of the tissue, and the velocity of insertion, steering angles must be calculated for individual insertions.

Subsequent work accounts for forces on the needle that cannot be modeled as components of the steering angle, such as dynamic friction and torsion in the needle shaft [24, 25]. These works still assume a constant steering angle, which implies that the needle is inserted into a homogeneous material. This assumption does not apply for most insertions into tissue, limiting the utility of the nonholonomic model for clinical applications.

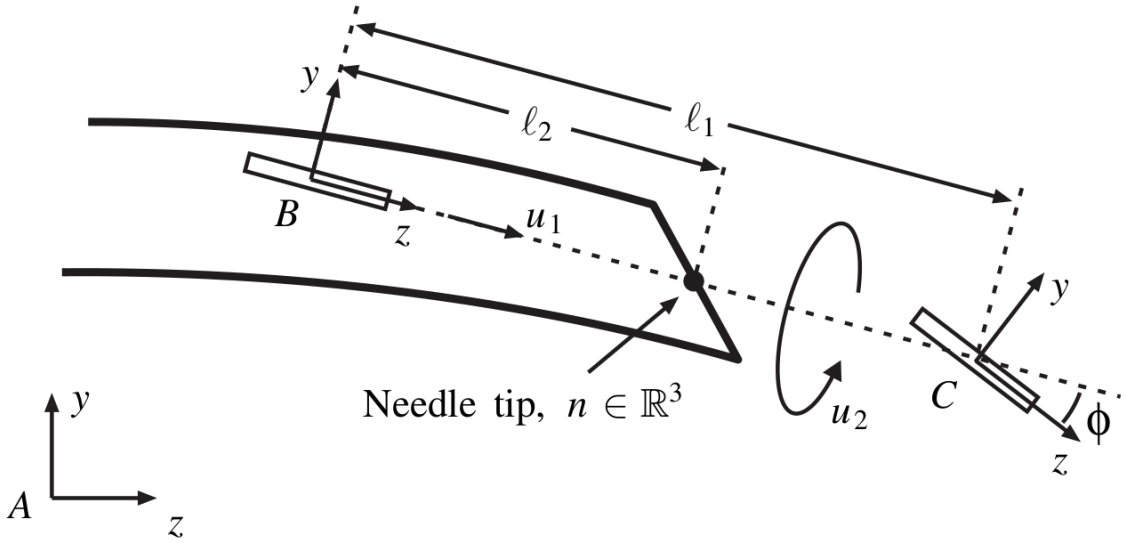


Figure 2.3: Nonholonomic model in which the needle tip is represented as a bicycle with a fixed front-wheel steering angle (from Webster, 2006 [4]).

2.2.2 Finite Element Models

Finite Element (FE) modeling of the needle and surrounding medium addresses some of the drawbacks of the kinematic needle model, such as the ability to model inconsistent deflection when inserting through nonhomogeneous tissue [5]. FEM-based approaches use several types of finite elements, including angular springs and beam elements. While the problem is often simplified as a 2D mesh in a plane, the approach is extensible to 3D [26].

FE modeling necessitates explicit representations for the sliding interface between the needle shaft and the surrounding tissue and for the elastic mechanical properties that govern the deformation of tissue during insertion [27]. Since needles are very slender and the magnitude of deflection is comparatively large, the assump-

tion of linear displacement usually used during FE analysis is not applicable and a computationally-intensive numerical solver is required to solve for nonlinear displacement.



Figure 2.4: Finite element model which represents the needle as a series of angular springs interacting with a 2D mesh [5].

2.2.3 Mechanical Models

Other works model the needle as an Euler-Bernoulli beam, with the forces acting on the needle divided into a force acting on the needle tip and a distributed load acting

on the needle shaft. The tip force is related to the force required to cut through the tissue, which depends on the insertion velocity [28]. The distributed shaft load is related to the stiffness and viscous coefficient of the tissue [29].

Another approach is to represent the shape of the needle as a polynomial and use mechanical bending energy to choose the polynomial coefficients [2, 7, 29]. This accounts for needle deflection and deformation of surrounding tissue, which allows calculation of the force on the needle base.

Mechanical models require direct measurement of the elastic modulus, stiffness, and cutting force of the tissue and the elastic modulus of the needle. The tissue is generally assumed to be homogeneous for simplicity.

2.3 Needle Steering

The different approaches to needle steering can be generalized as minimally-invasive methods to guide a needle to a desired point in the body using control inputs applied outside the body. The various methods produced in this line of research can be placed along a spectrum of mechanical complexity at the needle tip, ranging from methods for steering a needle using only control inputs at its base, to needles with some actuation at the tip and along the shaft, to continuum robots.

Needle steering strategies rely on the asymmetric force at the tip of a beveled needle as a control input to direct the needle along a desired trajectory. Rotating

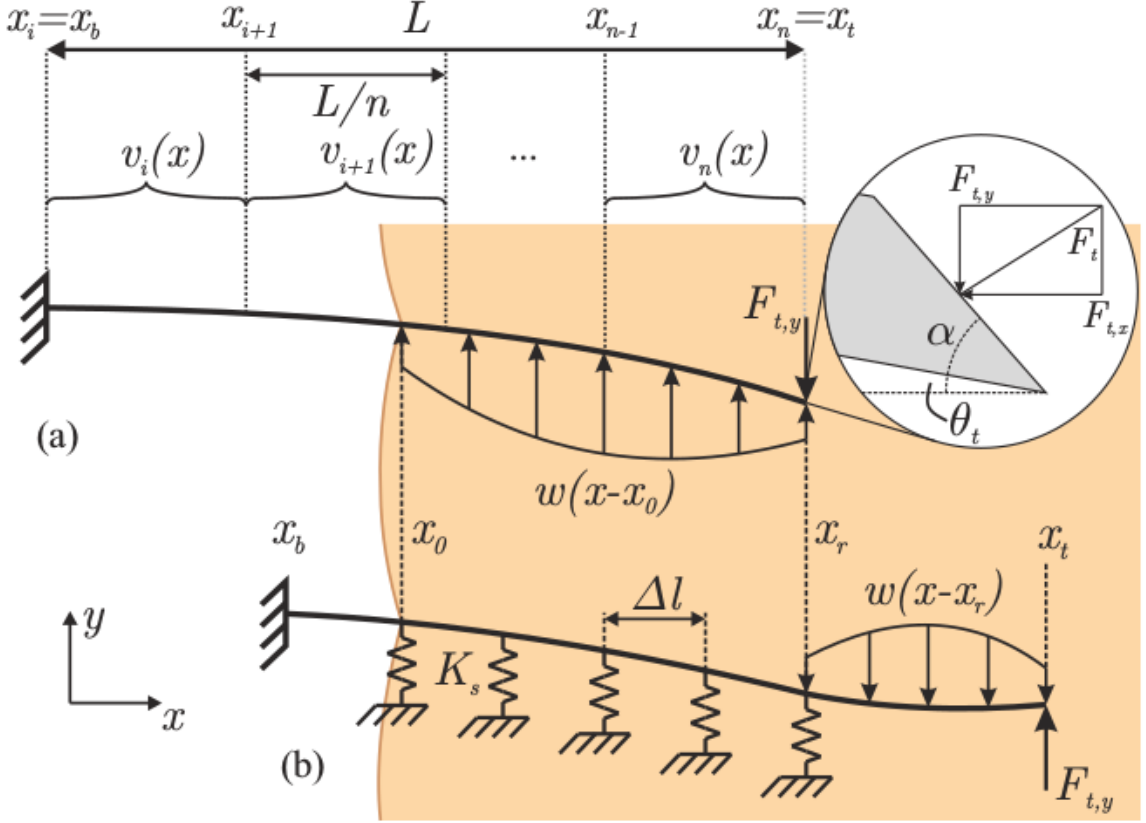


Figure 2.5: Mechanical model of a needle in a two-bend configuration (from Roesthuis, 2012 [3]).

the needle tip changes the direction of the force vector, allowing the direction of deflection to be controlled. Steering algorithms that take advantage of this behavior include duty cycle steering, CURV steering, and continuous-rotation steering.

Symmetric-tip needles are not subject to significant asymmetric tip forces during insertion [30]. While the magnitude of deflection during insertion is reduced, the direction of deflection is inconsistent, so symmetric-tipped needles cannot be steered by rotating the needle tip. An alternative strategy steers the needle by moving its base outside the tissue, which induces a bend in the needle shaft [31].

Curved- or kinked-tip needles use similar mechanical principles to steer as beveled-tip needles, but the addition of a pre-bent section greatly increases the asymmetric force applied to the needle tip during insertion [6]. This allows the needle to achieve a tighter turning radius, especially if the needle shaft is made of nitinol wire. Kinked-tip needles cause more tissue damage than beveled-tip needles when steered using a rotation-based strategy, but needles with passively-actuated tips have been developed to mitigate this by straightening during continuous rotation [32]. Needles with fully-actuated tips can be steered along a trajectory without rotating the needle [7]. A disadvantage of curved-tip needles is that the tip translates during rotation, which violates the assumption of the nonholonomic kinematic model that the needle will only move along the tip vector [6].

Concentric-tube needles consist of several nested pre-bent tubes [8, 33, 34]. An example with three concentric segments is shown in Figure 2.8. The needle can be actively curved or straightened by rotating the tubes so their directions of curvature are aligned or in opposition. These needles experience potentially-undesired releases of energy when the concentric elements snap between equilibrium states.

- Problems with these approaches, and with approaches that use custom needles in general, is that there aren't any clinically-available biopsy needles of these types. Need to be able to steer straight beveled-tip needles if we want to use what's out there right now.
- Potential for tissue damage along insertion trajectory is risky.



PLACEHOLDER

Figure 2.6: Example of a needle with a pre-curved tip [6].

2.4 Needle Localization

Existing work in needle localization generally operates on individual scans or video frames in isolation. It would be very useful to use the results from processing a previous image to find the needle in the current image. Adding the change in the forward kinematics of the needle would improve this process as well.

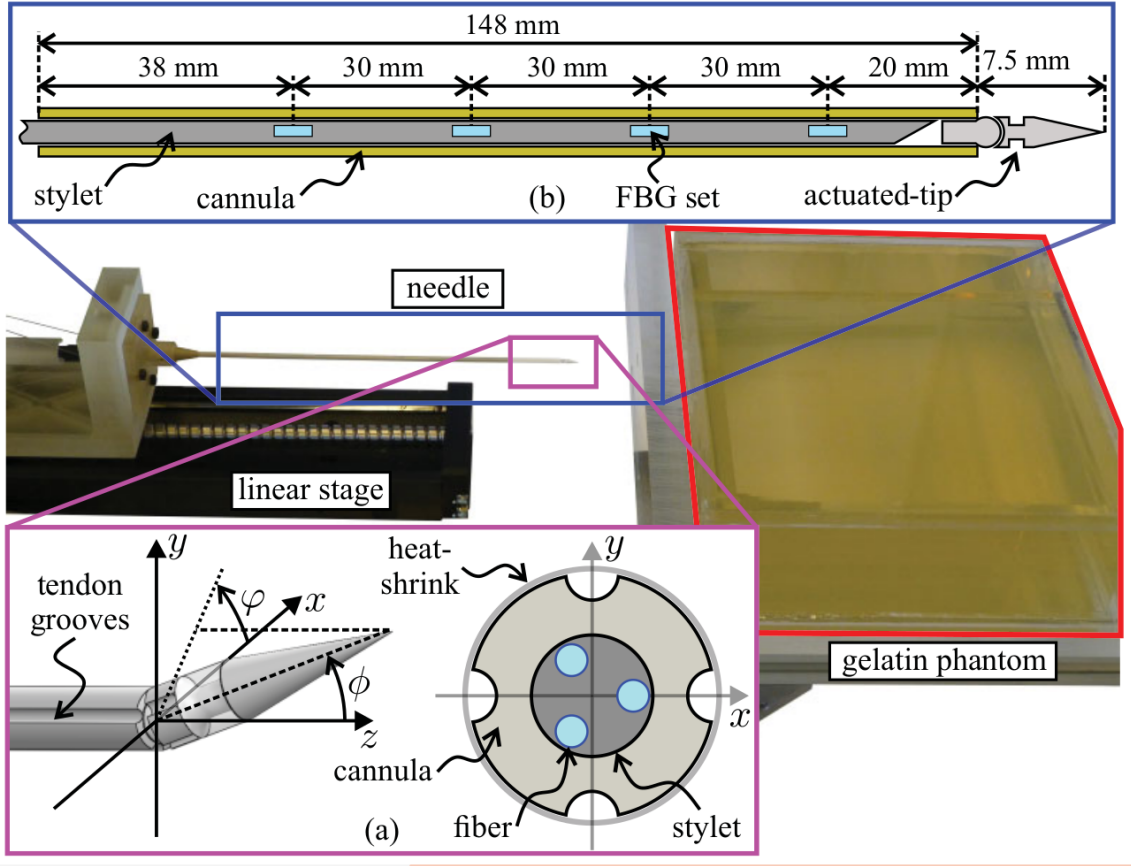


Figure 2.7: Custom-manufactured steerable needle with an actuated tip and Fiber Bragg Grating strain gauges (from Roesthuis, 2015 [7]).

2.4.1 Coronal and Sagittal Plane Imaging

Prior work by our research group demonstrated closed-loop MR imaging in the coronal and sagittal planes to follow the needle during insertion [9]. As shown in Figure 2.9, the needle tip is captured in each scan and its measured position of the centroid of the tip artifact is used to plan the pose of the subsequent scan in the perpendicular plane. The field of view of each plane is sized based on the maximum anticipated deflection of the needle between scans.



Figure 2.8: Example of a steerable concentric-tube needle with three concentric segments (from Rucker, 2010 [8]).

A major risk with this approach is the loss of tracking if the needle tip is not found in one of the scans because the key piece of information used to plan the position of each scan is the location of the needle tip in the immediately-previous scan. Since the scan planes are parallel to the needle shaft and could only be several millimeters thick, a small error in the placement of one scan plane could result in failure to capture the needle.^e This risk can be mitigated by making the thickness of the scan planes sufficient to capture the needle tip even if it deflects significantly between scans. However, high scan plane thickness reduces the clarity of features in MR images, which would be detrimental for identifying anatomical features near the needle.

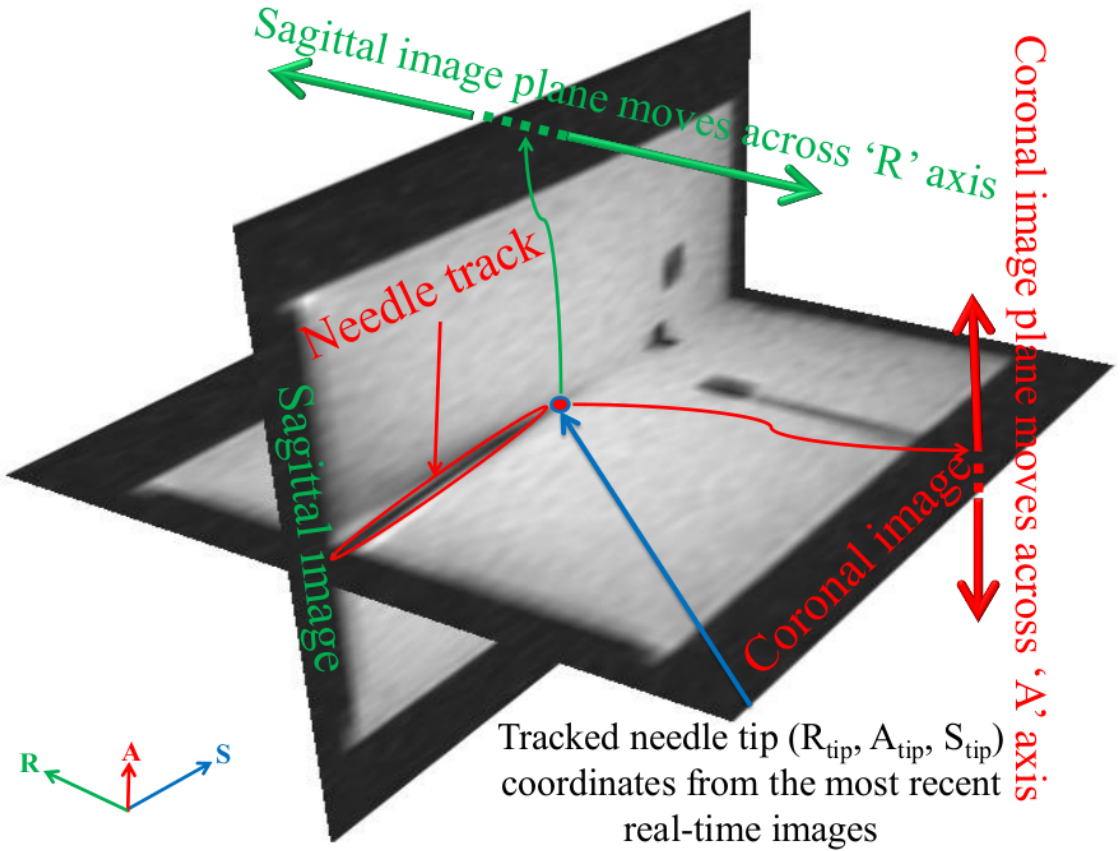


Figure 2.9: Alternating-planes strategy to track the needle tip during insertion (from Patel, 2015 [9]).

2.4.2 Transverse Plane Imaging

Imaging in the plane normal to the needle shaft captures the needle in cross-section. This avoids the problem of imaging in a plane that does not contain the needle, but it is more challenging to find the plane containing the needle tip. For US scanning [10, 35, 36], the transducer can be mounted on a motorized platform and moved in synchronization with the needle base to capture the same point on the needle in cross-section throughout insertion, as shown in Figure 2.10.

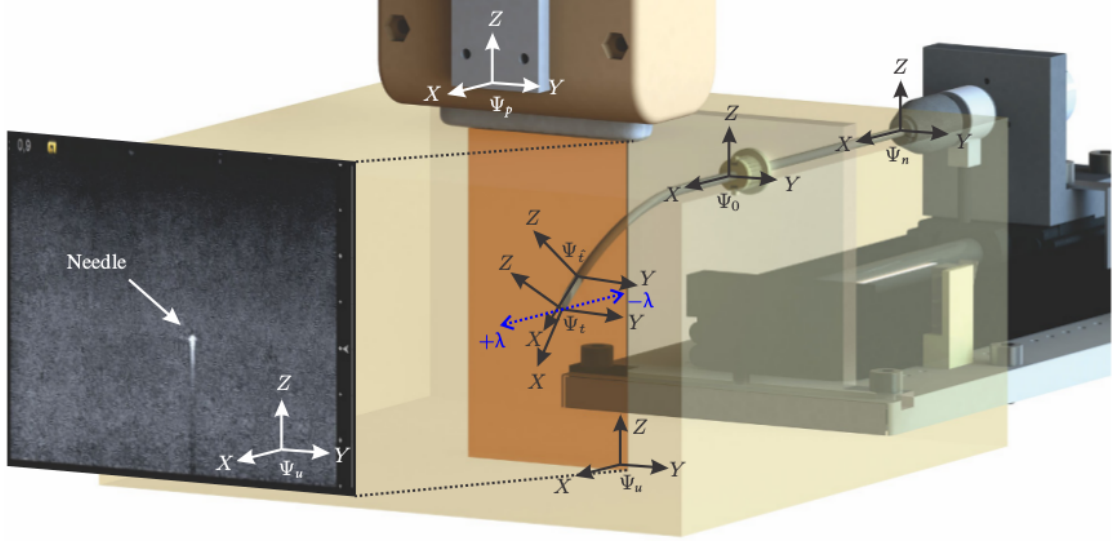


Figure 2.10: Needle tracking in US via imaging in the transverse plane (from Vrooijink, 2014 [10]).

2.4.3 3D Imaging

NeedleFinder is a 3D Slicer extension for needle localization and segmentation [11].

Figure 2.11 shows several catheters automatically segmented using NeedleFinder.

Given a manually-selected tip position, NeedleFinder searches through sequential axial scan planes and finds the cross-sections of the artifacts or voids in each layer. An angular-spring finite element model defined by the shape and stiffness of the needle is fit to the detected needle points. Manual selection of each needle tip is required because of the difficulty of automatically distinguishing each needle from anatomical features and noise in the MR images.

Other research models susceptibility artifact shapes for metal fiducial markers in MR data to automatically segment the markers and determine their poses [37]. This

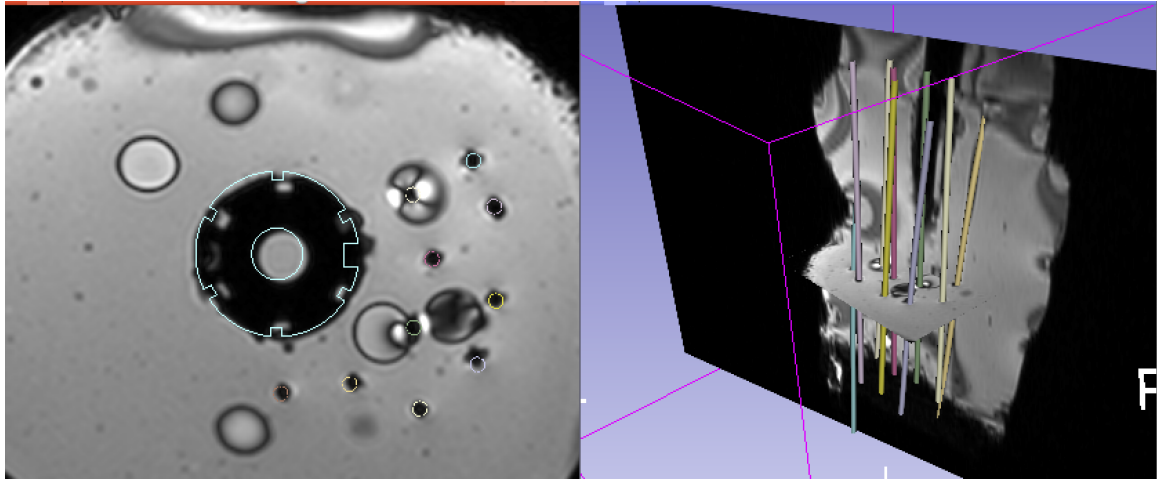


Figure 2.11: Catheters semi-automatically segmented in 3D MRI data using the NeedleFinder Slicer extension (from Pernelle, 2013 [11]).

approach could probably be extended to detect needle tip poses from tip artifacts with greater precision than thresholding by intensity, but the variation in the needle artifact with the orientation of the needle relative to the direction of the magnetic field would present some challenges.

In both US and MR images, the time required to resolve a 3D volume is higher than for a 2D plane, so 3D imaging is generally not suitable for real-time tracking or control.

2.4.4 Non-Imaging Techniques

An alternative method for detecting the position and shape of the needle is to add sensors to the needle to directly measure its deflection. One approach, shown in Figure 2.12 is to embed Fiber Bragg Grating optical sensors into the shaft of

the needle [12]. These sensors measure the strain in the needle as it bends and allow the shape of the needle to be calculated throughout insertion to achieve robotic steering. This approach requires specially-modified needles, precluding the use of common clinical-style biopsy needles.

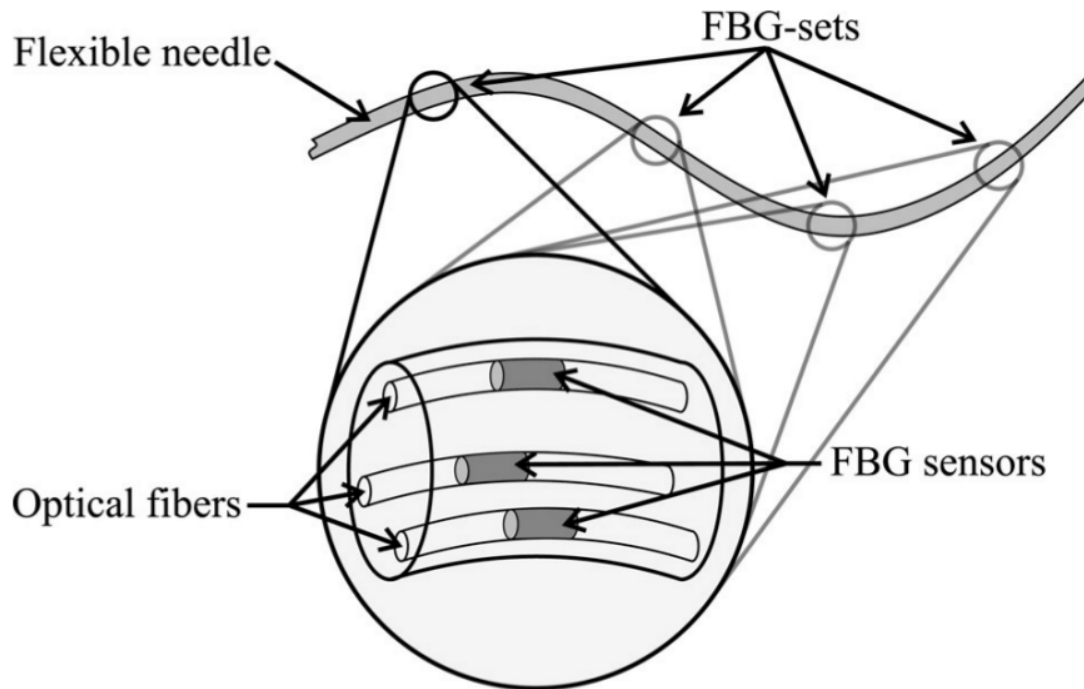


Figure 2.12: Placement of Fiber Bragg Grating sensors on a specially-modified needle (from Roesthuis, 2014 [12]).

Another option is to attach magnetic tracking coils to the needle shaft and use an external sensor unit like the Polaris to measure their 6-DOF poses and compute the needle shape. [38, 39] This isn't compatible with the MRI environment.

Chapter 3

Needle Model

The needle model presented in this thesis is based on minimizing the bending energy in the needle, which is represented as a beam and characterized as a parametric polynomial curve. Other existing needle modeling approaches account for bending energy, generally to determine the equilibrium state between the needle and the surrounding elastically-deformed tissue [2, 7, 29].

The model is initialized with the mechanical properties of the needle and updated throughout insertion with the most recent pose of the needle base and the latest observed points on the needle shaft. This allows estimation of the shape of the needle using only a few new images without requiring an explicit model of the forces acting on the needle.

Mechanics-based models make restrictive assumptions about the trajectory of the needle by limiting the number bends in the needle shaft [29]. Models that assume a

single direction of insertion preclude the trajectories achievable with highly-flexible needles. By parameterizing the needle coordinates independently of the insertion direction or depth, this model can represent needles inserted in any direction relative to the scanner coordinate frame.

Both nonholonomic kinematic models and mechanics-based beam bending models require extensive characterization of the properties of the needle and the tissue in order to accurately account for the tip and shaft loads placed on the needle. Tissue properties vary between tissue types and patients, and characterization of properties to the extent required by these models would probably not be possible to accomplish during a procedure. In contrast, this model does not require characterization of mechanical properties, since the constraints imposed on the needle by its interaction with surrounding tissue are measured through the observed shape of the needle.

In the context of MRI, it would be very time-consuming to exactly evaluate the state of the needle using only observations from imaging. The core idea of this model is to take a few observations and then optimize a model that meets those constraints and the constraints imposed by the mechanics of the needle. Provided that the constraints are carefully chosen, the needle model will be "close enough" to the actual state of the needle from the perspective of guiding insertion and planning future imagery.

3.1 Assumptions

As currently formulated, this model only considers straight needles with uniform stiffness and cross-section. Actuated devices such as flexible-tip needles and continuum robots are not considered. It is also assumed that the state of the needle can be observed in imaging.

The model uses the following information about the composition and state of the needle:

- 6-degree-of-freedom pose of the base of the needle, via the forward kinematics of the insertion robot
- Length of the needle
- Diameter of the needle
- Elastic modulus of the needle
- Multiple observed coordinates on the needle shaft from a sparse set of cross-sectional images

Definitions of the symbols used in the needle model are provided below.

Symbol	Description
U_B	mechanical bending energy
L	needle length
d	needle diameter
s	parametric variable
n	polynomial degree
δ	needle tip offset
ρ	needle curvature
ϵ	needle curve error threshold
k	observation index
E	elastic modulus
I	second area moment of inertia
$x \in X$	X-component , set of X-components of needle coordinate
$y \in Y$	Y-component , set of Y-components of needle coordinate
$z \in Z$	Z-component , set of Z-components of needle coordinate
v	magnitude of deflection relative to the needle neutral axis
\mathbf{V}	vector, needle coordinate
C	cumulative cost of the needle model configuration

3.2 Beam Bending Energy

The actual biopsy needle contains several parts with different mechanical properties, such as an inner rod that slides within an outer shell. Since these interactions are computationally expensive to model exactly and unnecessary to account for unless a very high degree of fidelity is desired, the model presented here simplifies the needle as a solid cylindrical beam and neglects the change in cross-sectional area at the needle tip. Under these assumptions the area moment of inertia of the needle in cross-section is constant along its entire length and can be written as Equation 3.1.

$$I = \frac{\pi}{64}d^4 \quad (3.1)$$

Since the needle is assumed to have a constant diameter along its entire length, it can be represented as an Euler-Bernoulli beam with constant cross-sectional area. The transverse bending energy in a straight beam with constant cross-section, shown in Equation 3.2, is a function of the curvature in the beam integrated over its length. Equation 3.3 shows the calculation of curvature in an arc.

$$U_B = \frac{EI}{2} \int_0^L \frac{1}{\rho^2} dl \quad (3.2)$$

$$\frac{1}{\rho} = \frac{d^2v/dl^2}{(1 + (dv/dl)^2)^{3/2}} \simeq \frac{d^2v}{dl^2} \quad (3.3)$$

In a beam subject to zero load its cumulative curvature is zero, so its total bending energy is also zero. Higher curvatures correspond to sharper bends, which means that a beam that is predominately straight with one very sharp bend will have a greater bending energy than a beam of the same length where the bend is gentle and distributed along its entire length. Beams adopt shapes that minimize their cumulative bending energy while meeting constraints imposed by external fixtures.

3.3 Parametric Polynomial Space Curves

The needle curve is represented using an n -degree parametric polynomial function, shown in Equation 3.4.

In the context of representing a needle, n represents the maximum number of inflection points in each axis. A needle inserted without rotation would deflect consistently in one direction and its shape could be represented using at minimum a 3rd-degree polynomial ($n = 3$).

$$\mathbf{V} = \begin{bmatrix} x(s) \\ y(s) \\ z(s) \end{bmatrix} = \begin{bmatrix} a_n s^n + a_{n-1} s^{n-1} + \dots + a_1 s + a_0 \\ b_n s^n + b_{n-1} s^{n-1} + \dots + b_1 s + b_0 \\ c_n s^n + c_{n-1} s^{n-1} + \dots + c_1 s + c_0 \end{bmatrix} s \in (0, 1) \quad (3.4)$$

The three spatial coordinates x , y , and z are functions of a unitless parameter s , which ranges from 0 at the needle base to 1 at the needle tip. Given sets of needle coordinates X , Y , and Z , the relationship between the values of s and the positions of

the needle coordinates is established by the distances between the needle coordinates, calculated in Equation 3.5, and the proportion of each distance to the cumulative distance between all the coordinates, calculate in Equation 3.6.

$$\begin{cases} d_k = 0 & \text{if } k = 0 \\ d_k = |\mathbf{V}_k - \mathbf{V}_{k-1}| & \text{if } k > 0 \end{cases} \quad (3.5)$$

$$\begin{cases} s_k = 0 & \text{if } k = 0 \\ s_k = s_{k-1} + \frac{d_k}{L_{needle}} & \text{if } k > 0 \end{cases} \quad (3.6)$$

While an alternative implementation could represent the x - and y -components of the coordinate as a function of the z -component, using an independent parameter allows the curve to represent torturous trajectories without placing restrictions on the direction of needle insertion.

The maximum number of inflection points in each axis, and consequently the maximum number of changes in needle direction that the curve can represent, is limited by the degree of the polynomial.

3.4 Curve Fitting

The purpose of curve fitting is to choose coefficients of the parametric function in Equation ?? given a number of observed needle cross section coordinates so that

the total bending energy in the curve and the error between the curve and the needle coordinates are minimized.

Prior to optimization, initial coefficients for each curve are found by fitting a polynomial of degree n to the needle coordinates using least-squares. While this initial solution is not representative of the actual mechanical factors that determine the shape of the needle, it approximates the minimum bending energy curve and helps prevent the optimization for reaching a local minimum or other failure condition.

The curve is optimized to minimize bending energy using Sequential Least SQuares Programming (SLSQP), which is an iterative constrained Non-Linear Programming (NLP) search algorithm [40].

3.4.1 Cost Function

The cost function subject to minimization is shown in Equation 3.7. It is a modification of Equation 3.2 where the elastic modulus and area moment of inertia are omitted, since they are constant along the length of a straight needle with uniform cross-section.

$$C = \int_0^L \frac{1}{\rho^2} dl \quad (3.7)$$

3.4.2 Constraints

The optimization is constrained by Equation 3.8 such that the coordinates of the curve at $t=0$ matches the position of the base of the needle.

$$\mathbf{V}_{k=0} = \begin{bmatrix} a_0 \\ b_0 \\ c_0 \end{bmatrix} \quad (3.8)$$

The optimization is further constrained by Equation 3.9 so that the length of the curve between $t=0$ and $t=1$ is equal to the length of the needle and by Equation 3.10 so that the root-sum-mean error between the curve and the observed points is below a specified threshold ϵ .

$$L = \int_0^1 \left| \frac{d\mathbf{V}}{ds} \right| ds \quad (3.9)$$

$$\epsilon \geq \sqrt{\frac{\sum_{i=0}^k (V_i - V_{i,obs})^2}{k}} \quad (3.10)$$

While equality constraints can also be used to guide the optimized curve to intersect all the needle coordinates, this approach risks over-constraining the curve where the degree of the polynomial is close to the number of equality constraints.

3.4.3 Assumptions

Equations 3.5 and 3.6 assumes that length of the needle model curve is close to the sum of the distances between the sampled points on the needle. This is met if the deflection of the needle tip throughout insertion is be comparatively small and the number of sample points is be sufficient to characterize the shape of the needle.

3.5 Software Implementation

Algorithm 1 shows the process of calculating polynomial coefficient to minimize bending energy given a set of observed needle coordinates. Figures 3.1, 3.2, and 3.3 show the process of observing points near the modeled needle curve and optimizing a new curve to match them.

Algorithm 1 Curve Optimization

```
1: procedure UPDATE CURVE FIT( $coords_{needle}, L_{needle}, poly_{prev}$ )
2:    $t \leftarrow CalculateParameters(coords_{needle}, L_{needle})$ 
3:   if  $poly_{prev}$  is None then
4:      $poly_{init} \leftarrow LeastSquares(coords_{needle})$ 
5:   else
6:      $poly_{init} \leftarrow poly_{prev}$ 
7:    $cons \leftarrow DefineConstraints(t, coords_{needle}, L_{needle})$ 
8:    $poly_{opt} \leftarrow DoOptimization(poly_{init}, cons)$ 
9:   return  $poly_{opt}$ 
```

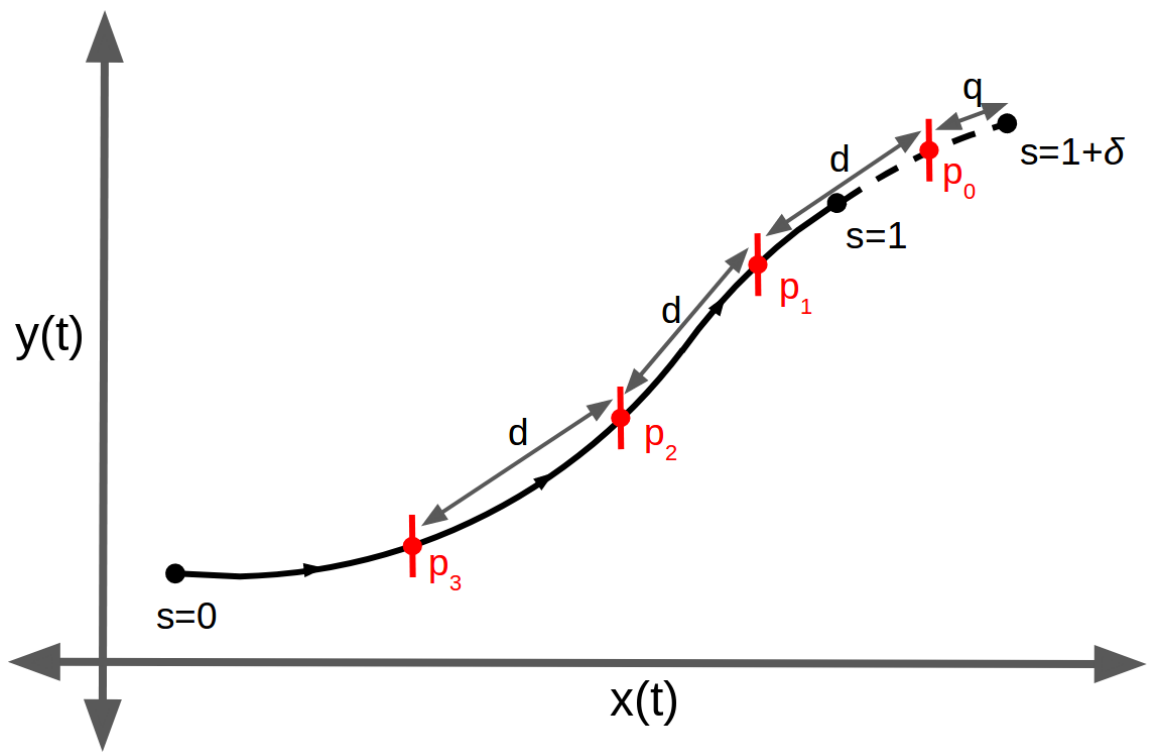


Figure 3.1: Given a number of samples, the spacing between the samples, an offset distance from the needle tip, and a new needle base pose, the expected coordinate of the needle is calculated at each sample point.

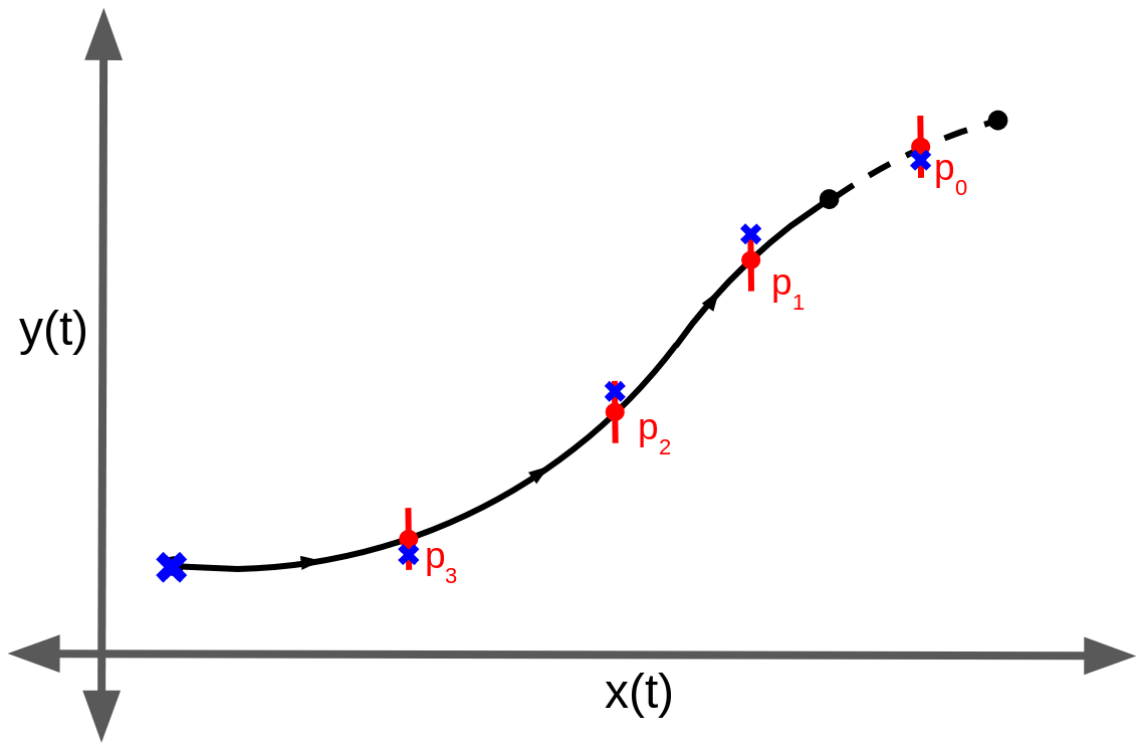


Figure 3.2: New imaging is collected at each needle coordinate, and the actual position of the needle is observed.

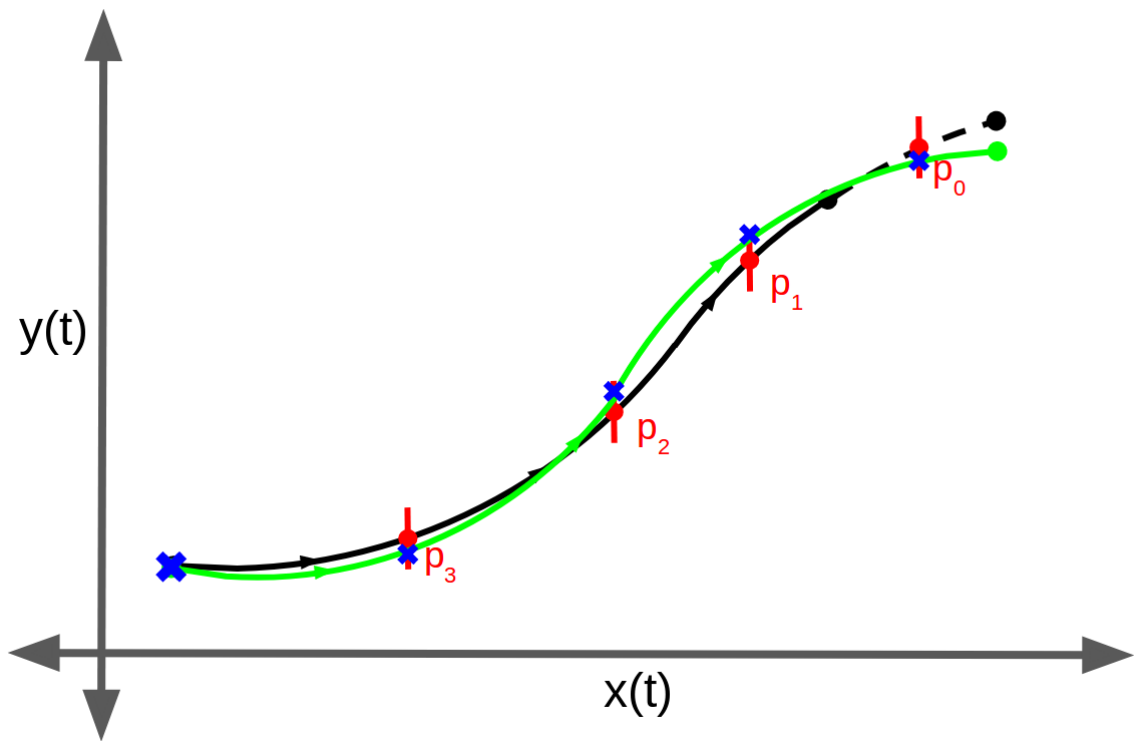


Figure 3.3: A new polynomial curve is calculated, optimized to minimize both the cumulative bending energy in the needle and the error between the curve and the observed points.

Chapter 4

Needle Localization in MR Images

4.1 Software Architecture

4.1.1 Simulated MRI Scanner

Full 3D MRI volumes take a long time to produce, especially if high resolution is desired: the scan time for each volume used in this thesis was approximately 5 minutes. This is a prohibitively long time in the context of real-time intraoperative imaging, so the MRI would be configured to provide 2D scans in requested planes with limited field of view. To simulate this functionality, a Slicer module was created to resection 2D slices from each 3D volumes at specified depths.

4.1.2 Needle Tracking Module

A second Slicer module manages the needle tracking process. Figure 4.1 shows the architecture of this module relative to the Slicer environment and the needle modeling utility. A linear transform node is set to match the pose of the needle base in each saved volume. When commanded by the operator, the module requests slices of the MRI volume at evenly-spaced coordinates along the shaft of the needle. The thresholded image is grouped into contiguous regions, and the area and centroid are calculated for each region. The region with the centroid closest to the estimated position of the needle provided by the previous needle model curve is assumed to be the needle artifact, and the position of its centroid determines the observed position of the needle in this image. The position of the needle base is appended to this list of needle coordinates, and the combined list is used as one of the inputs for the needle curve optimization.

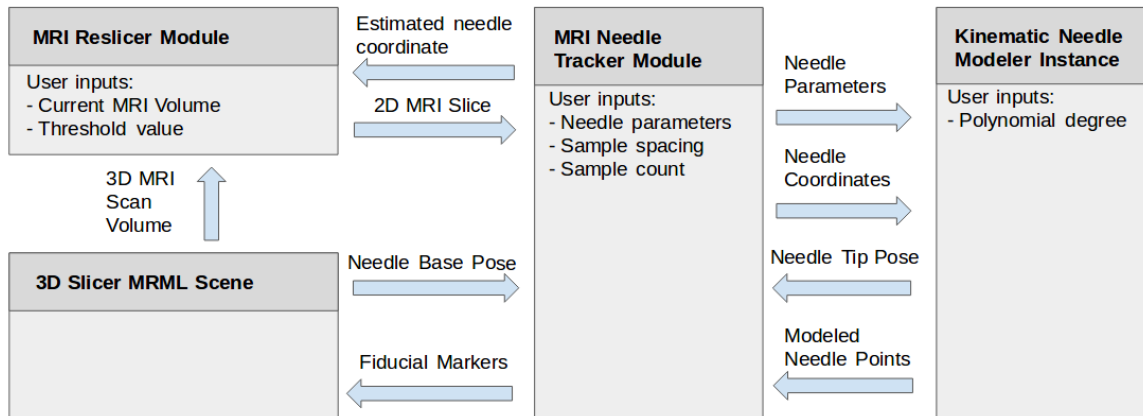


Figure 4.1: System architecture for needle detection and modeling from MRI data.

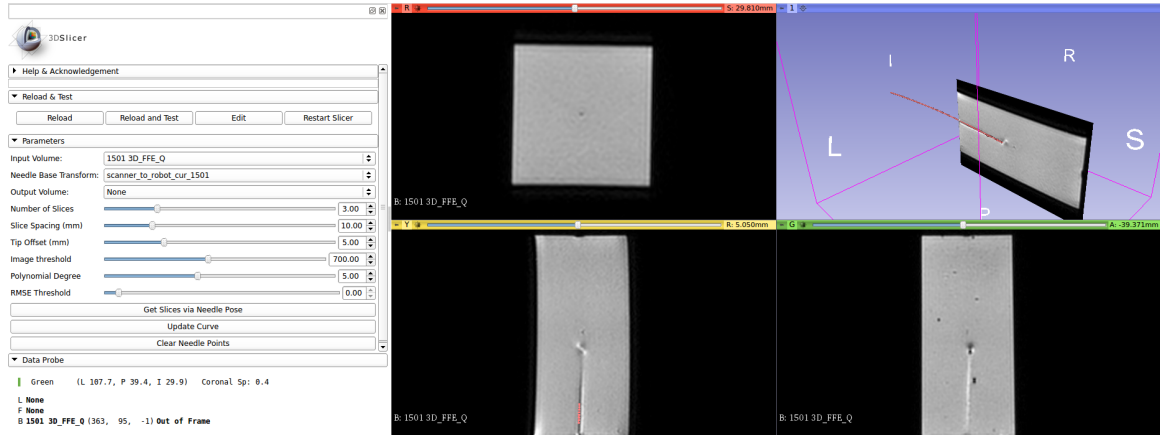


Figure 4.2: User interface for MRINeedleTipTracker 3D Slicer module.

4.2 Experiment

The purpose of this experiment is to validate the parametric curve fit and needle model on imagery representative of what would be available from intraoperative imagery during an MRI-guided insertion.

Several assumptions made to reduce the complexity of the experiment and facilitate needle tracking are listed below.

- A single beveled-tip clinical-style biopsy needle is to be inserted and tracked.
- The initial vector of the needle is normal to the axial plane, and the actual pose of the needle base exactly matches the recorded pose.
- Only homogeneous gelatin tissue phantoms are considered. The problem of identifying the needle in the presence of anatomy or other clutter is not addressed.

- New MR data is acquired and transmitted instantaneously.

4.2.1 MRI Data Collection

The set of MRI volumes used in this experiment was captured in the 3T scanner at UMass Medical Center using a 3D Fast Field Echo protocol. The dimensions of each voxel are 0.4mm x 0.4mm x 0.5mm. The phantom used was made of agar gelatin. The needle was a 150mm stainless steel ($E = 200$ GPa) clinical-style biopsy needle with a beveled tip and a diameter of 2mm. Removable plastic spacers with a thickness of 5.95mm regulated the insertion distance. Two spacers were removed between scans, so the needle moves in increments of 11.9mm. Five scans were collected in total. The plastic alignment frame shown in Figure 4.3 kept the needle aligned along a known vector relative to the phantom. When used in conjunction the alignment frame and spacers allow the 6-DOF pose of the needle base to be calculated in each scan without the use of a Z-frame or external tracking equipment.

4.2.2 Needle Localization

Each volume was thresholded at intensity 1500 to isolate the needle artifact. The segmentation labelmap was exported and processed separately.

The MRI volumes for each insertion step were loaded in sequence and a linear transform was set to match the pose of the needle base at each step. The needle

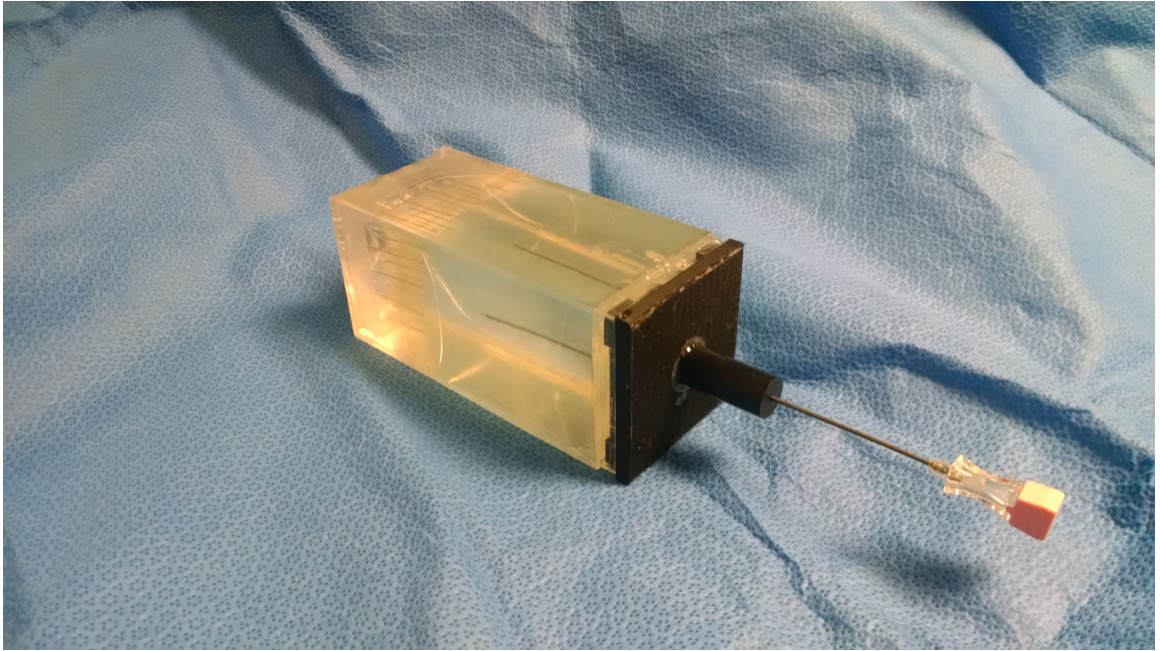


Figure 4.3: Tissue phantom with needle alignment frame and biopsy needle.

localization algorithm was run on each dataset in turn to generate an array of points representing the simulated needle.

4.3 Results

The baseline for the position of the needle shaft in the phantom was established by segmenting the needle artifact by intensity and computing the centroid of its cross section in every axial scan slice. Figure 4.4 shows the segmentation for the final step of the insertion, and Figure 4.5 shows the positions of the centroids in successive axial planes. The error for each model is computed as the difference between the centroid coordinate and the modeled coordinate in each slice.

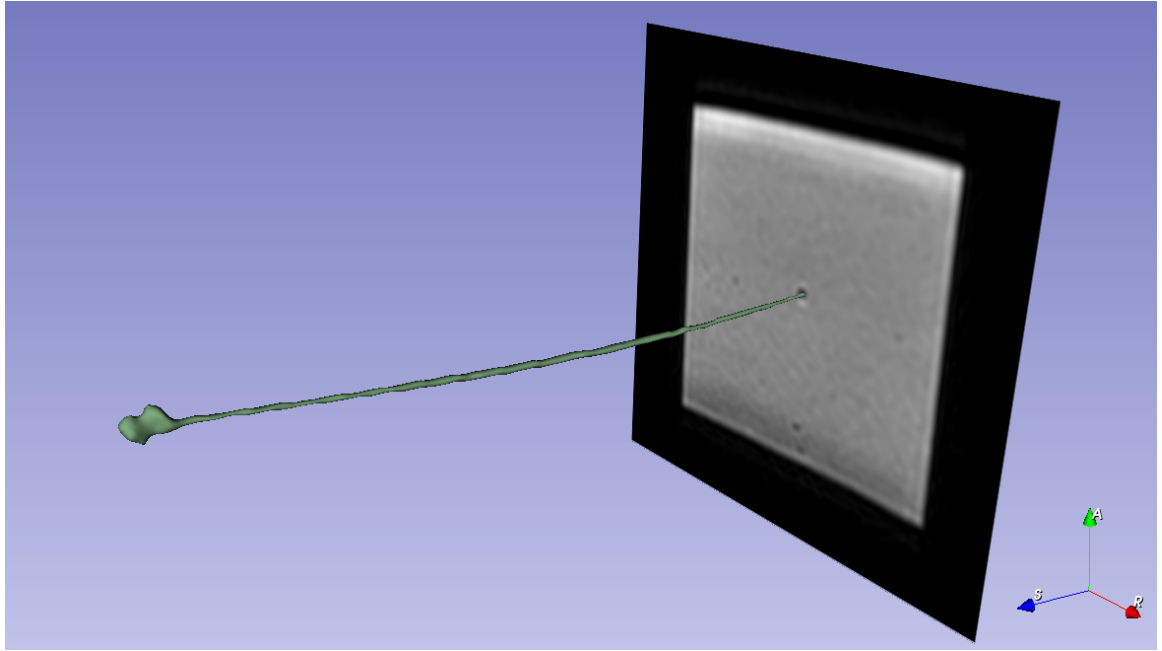


Figure 4.4: Segmentation of needle artifact generated by thresholding MRI volume.

4.3.1 Needle Localization at a Single Timestep

At the start of curve optimization using data from an individual insertion step the needle is assumed to be a vector with magnitude matching the length of the needle. The sampling locations are offset from the estimated position of the needle tip by a user-configurable distance to avoid sampling points within the tip artifact.

Figure 4.6 shows the relative error using a 1st-, 3rd-, 5th-, and 7th-degree polynomials. The tip offset $\delta = 5.0\text{mm}$, the sample spacing $d = 26.0\text{mm}$, and the number of observed slices $k = 3$.

Figure 4.7 show the effect on error relative to baseline as the number of slices observed over the length of the needle is increased.

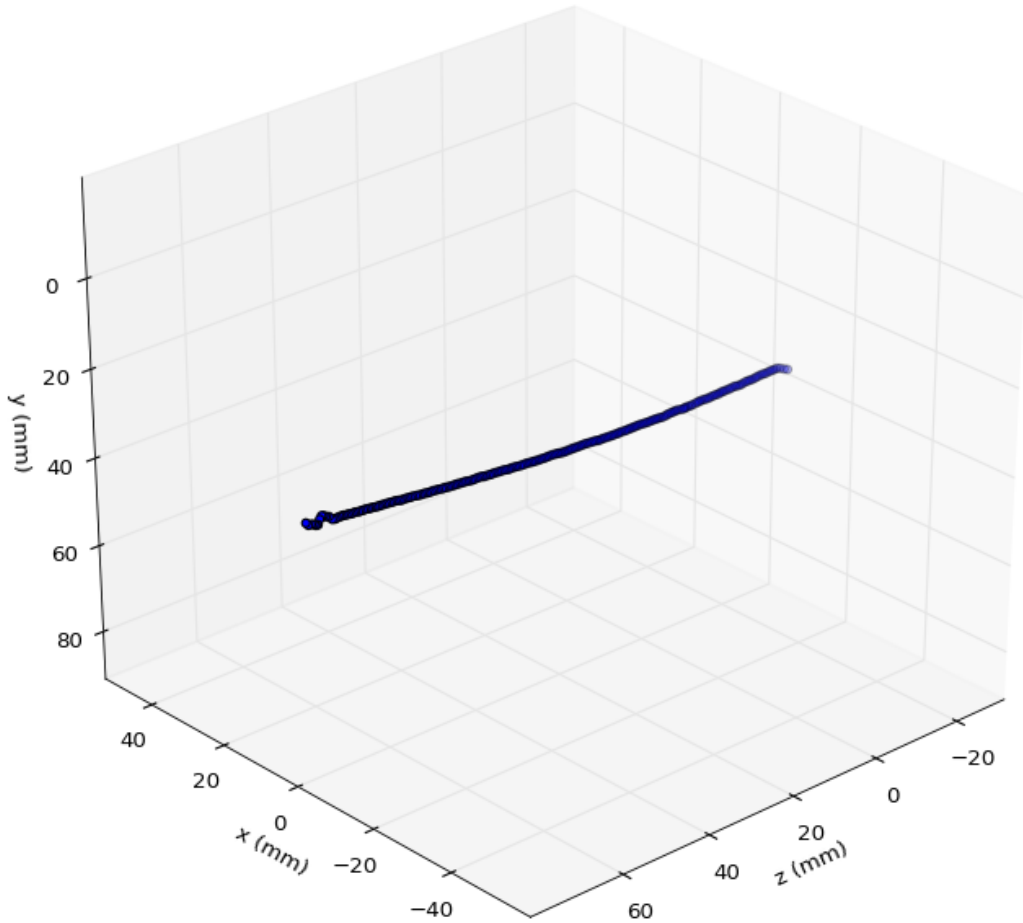


Figure 4.5: Baseline ground truth data, calculated from the centroids of the segmented artifact sectioned in the X-Y plane.

4.3.2 Needle Localization at Sequential Timesteps

Needle tracking in a sequence of images consists of repeated application of the method for an individual timestep described in 4.3.1. The optimized curve from the previous localization step is used as the initial estimate for the next localization step. The curve was a 5th-degree polynomial. Three slice planes were selected, starting 5mm from the tip and spaced 10mm apart.

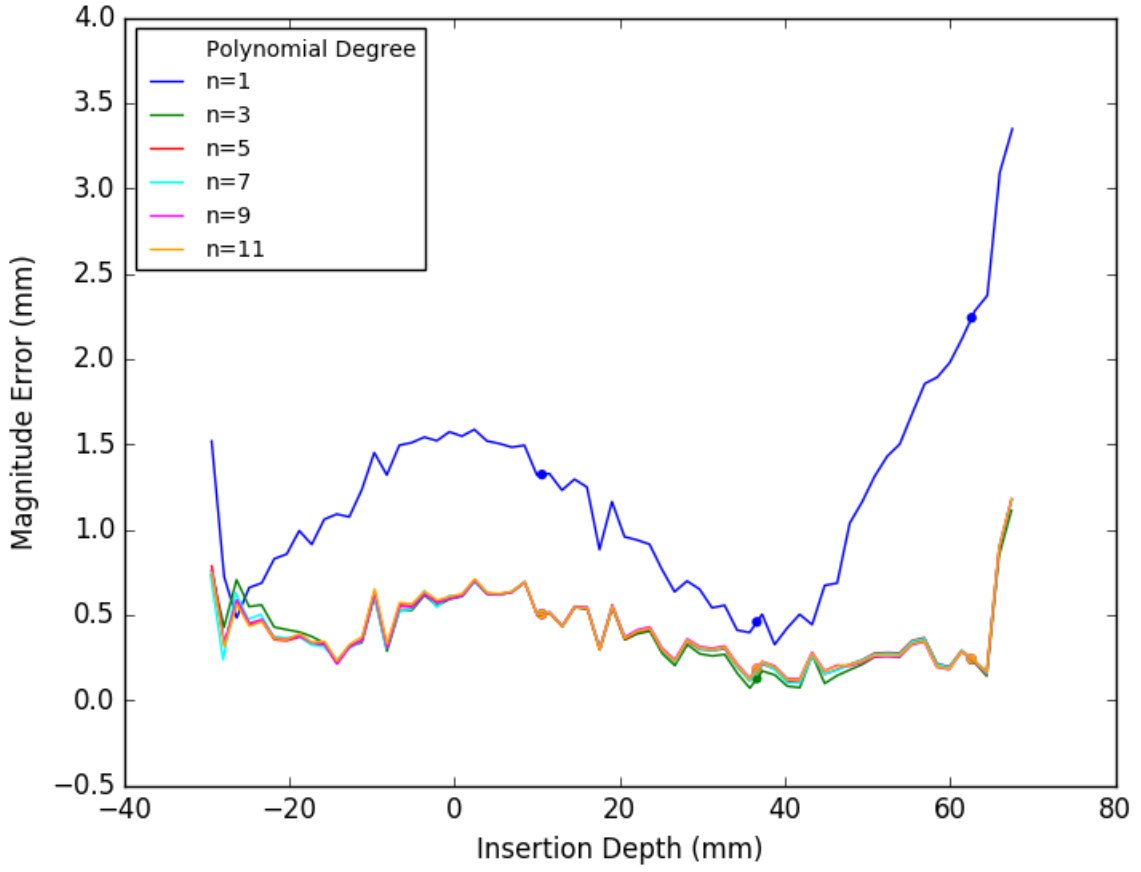


Figure 4.6: Magnitude of in-plane error over insertion for various degrees of polynomial. Markers indicate the positions of the slices on the needle curve. $d = 26.0\text{mm}$, $k = 3$, $\delta = 5.0\text{mm}$

Figure 4.9 shows the positions of the scan planes and Figure 4.10 shows points along the optimized curve for each insertion interval. Figure 4.11 shows the magnitude of error relative to the baseline for the optimized curve at each interval. Figure 4.12 shows the magnitude of error when the spacing between the slices is increased as the needle is inserted.

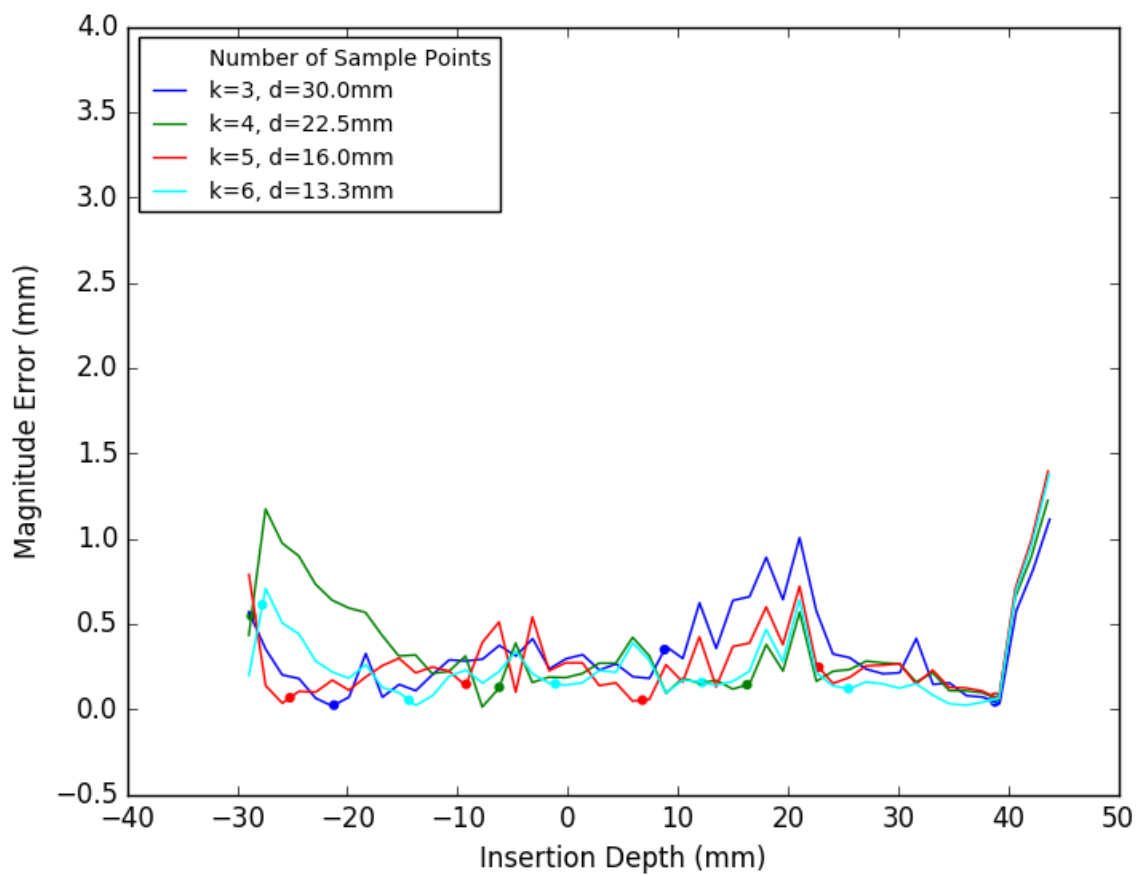


Figure 4.7: Magnitude of in-plane error over insertion for a variable number of sample points. $n = 5$, $\delta = 5.0\text{mm}$



PLACEHOLDER

Figure 4.8: Example polynomial curve fit plotted against the positions of the artifact centroids in transverse plane.

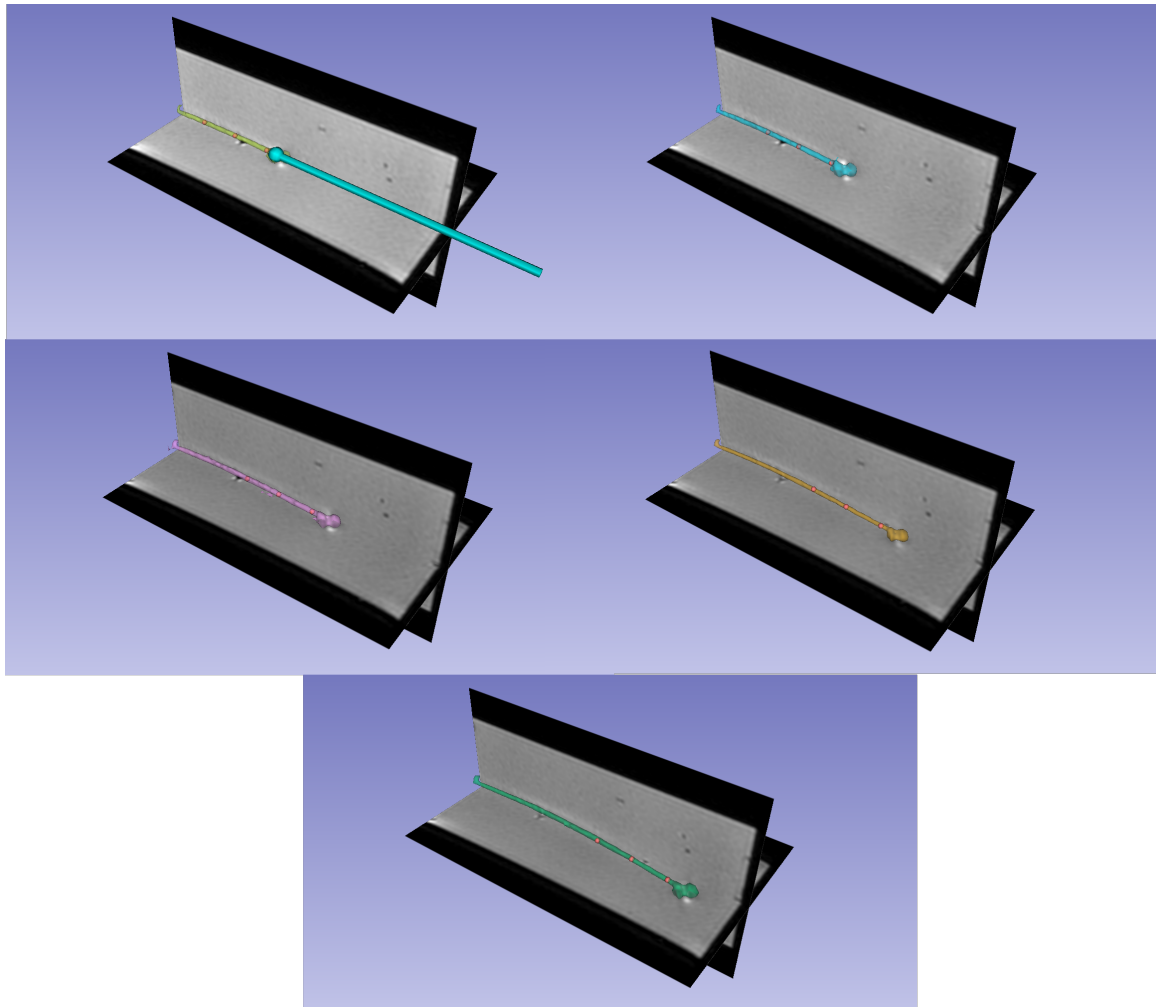


Figure 4.9: Positions of 2D scan planes at each insertion step, with segmented artifact.

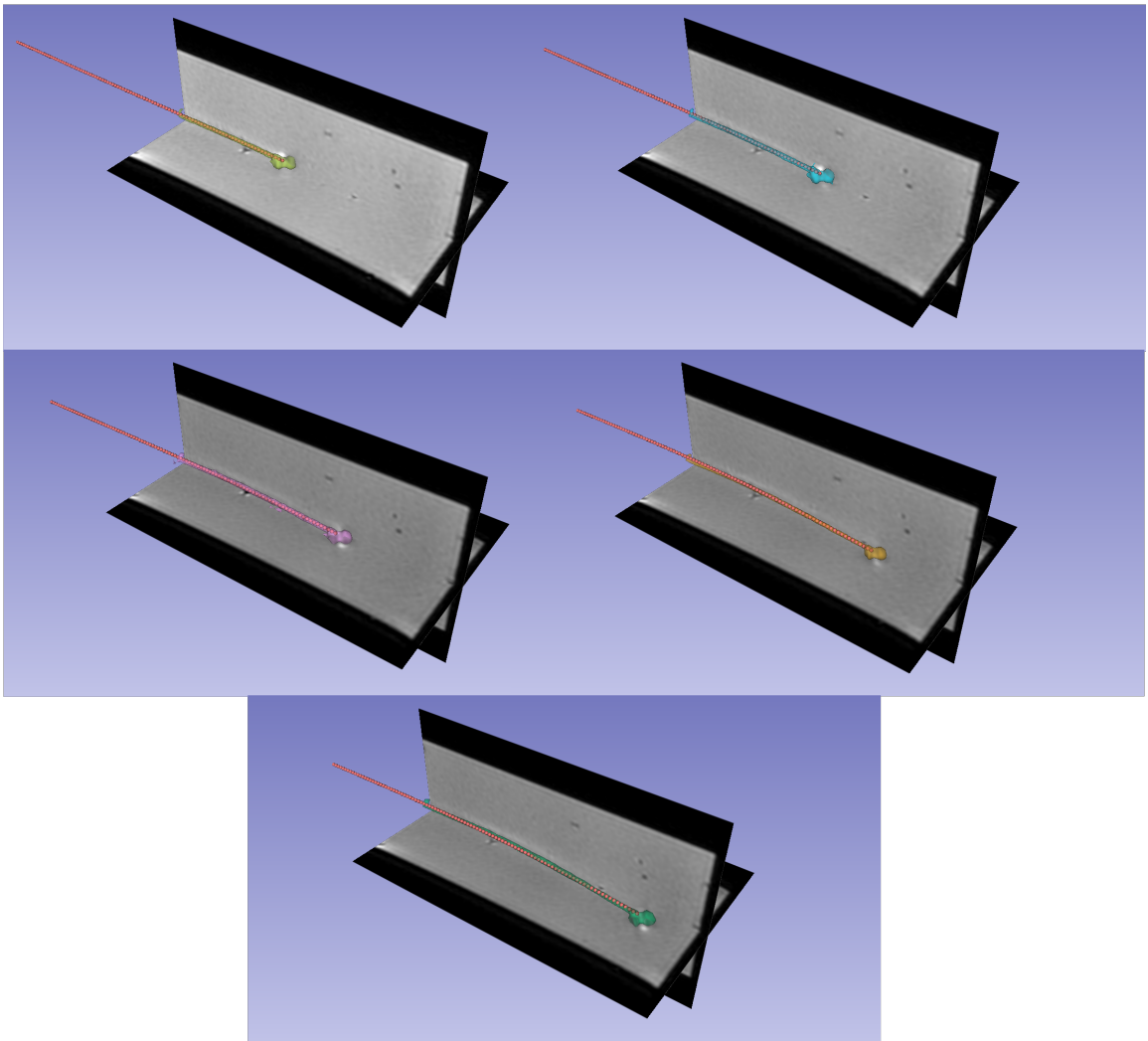


Figure 4.10: Modeled curve points at each insertion step, with segmented artifact.

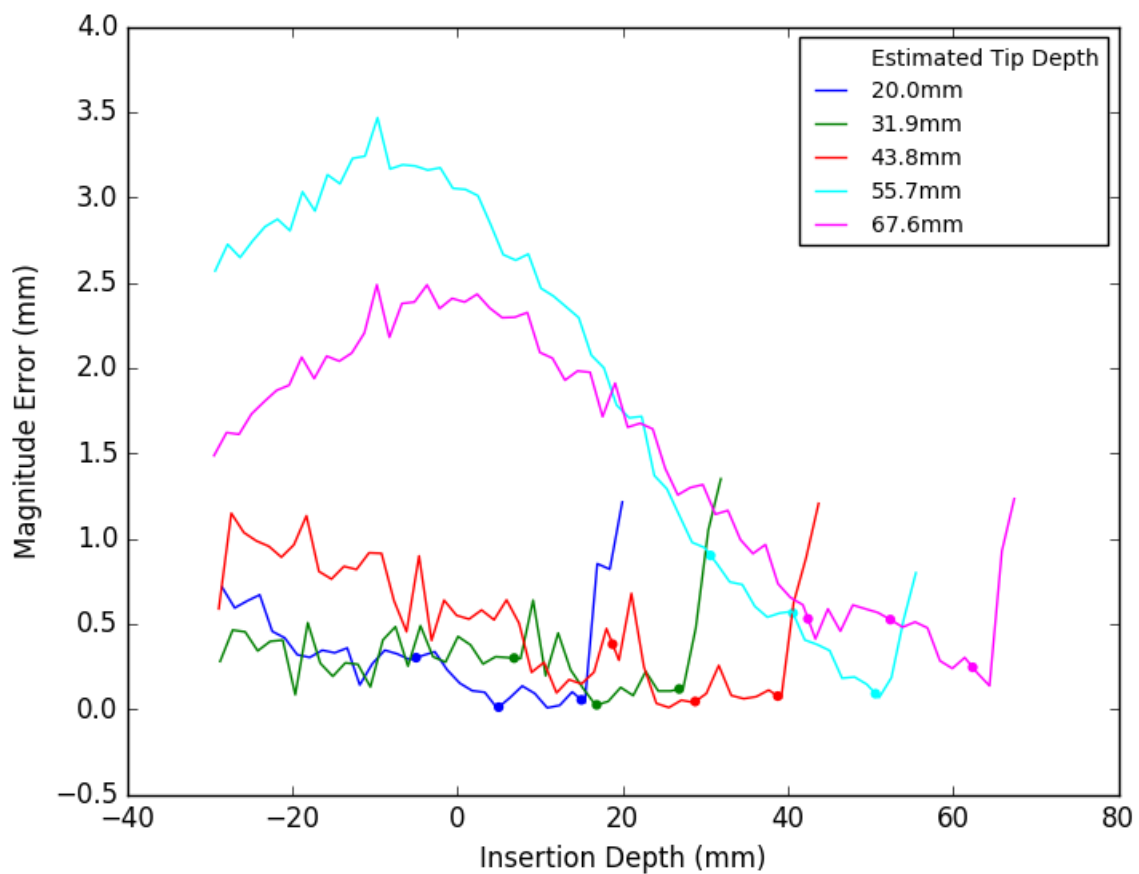


Figure 4.11: Magnitude of error between the needle model and the artifact centroid.
 $d = 10\text{mm}$, $k = 3$, $\delta = 5\text{mm}$

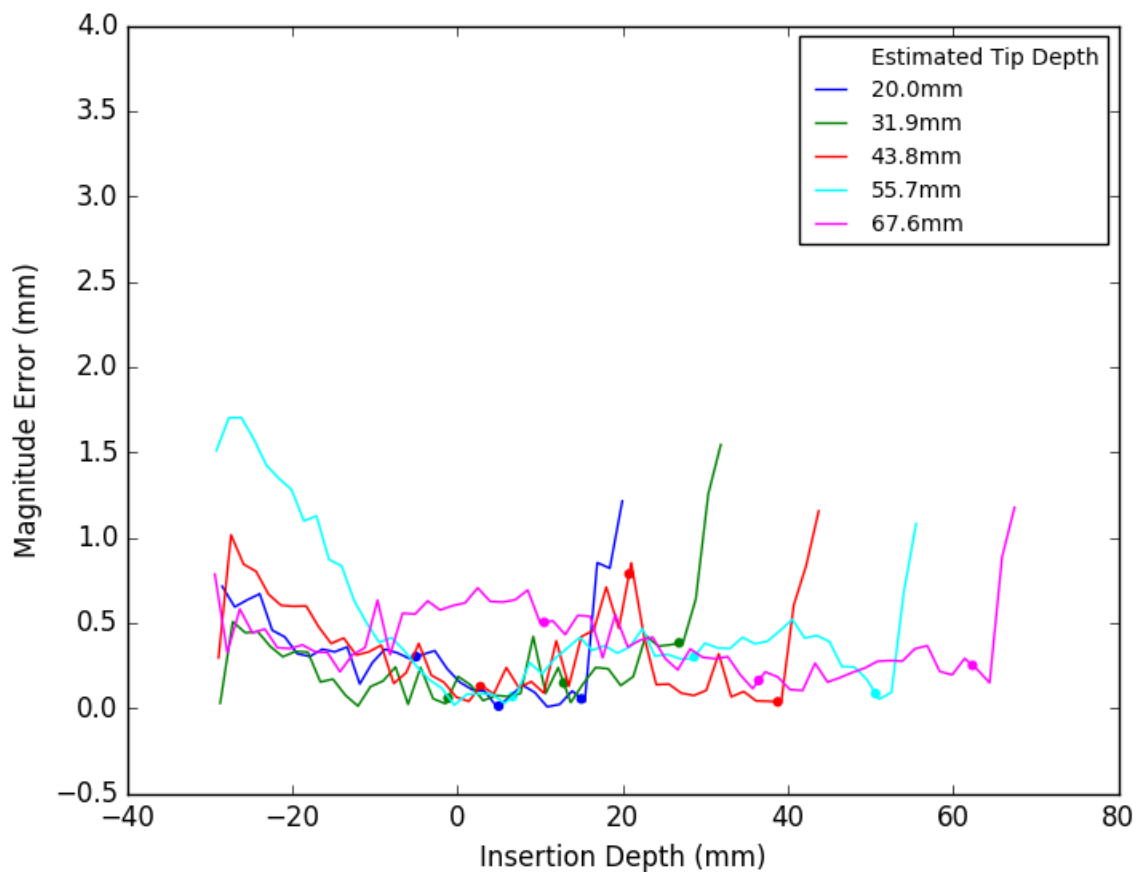


Figure 4.12: Magnitude of error between the needle model and the artifact centroid, where the spacing between each slice increases with insertion depth. $d = 10\text{mm} + \text{index}_{\text{step}} * 4\text{mm}$, $k = 3$, $\delta = 5\text{mm}$

Chapter 5

Discussion and Conclusion

5.1 Discussion

5.1.1 MRI Experiment

The experimental results show that important parts of closed-loop model-guided needle localization work in conjunction. The needle artifact centroids are all correctly identified by using the closest thresholded region to the estimated needle position in the scan, even when other large non-needle artifacts are present.

The length constraint allows the needle curve to extend beyond the furthest sampled point into the tip artifact region.

The error relative to the artifact cross-section centroid outside the tip artifact region is less than 0.5mm, which is comparable to other work in needle localization

in US [36] and MRI [22]. The error is high in the tip artifact region because the artifact is lopsided and its centroid is not located on the needle shaft, but this is a shortcoming in the baseline dataset and does not reflect the error relative to the actual position of the needle. Extending the dataset to include a CT scan at each needle insertion step would provide a superior baseline along the entire length of the needle.

The linear model exhibits significant error relative to the baseline and misrepresents the shape of the needle for a majority of its length. Choosing a high-degree polynomial does not produce a significant reduction in error since the needle trajectory in the MRI dataset exhibited deflection only in one direction.

Increasing the number of observation points along the length of the needle does not reduce the error relative to the baseline, provided that the points are spaced evenly along the portion of the needle visible in imaging.

In general, the concept of modeling the needle shape by sampling needle cross-sections in MRI is sound and could be extended for real-time applications.

5.1.2 Needle Model

The bending energy model is able to produce a good fit for the needle with very few sampled points. It does not over-fit, even when the small number of sample points would otherwise underconstrain the model. The curve between sample points approximately matches the actual position of the needle.

Optimization takes a long time to converge to a solution, between 5 to 10 seconds depending on the constraints (Lenovo ThinkPad P50, Intel Xeon CPU E3-1505M v5 @ 2.80GHz, 16 GB RAM). Constraints on the needle length and the average error contribute to increased processing time. This is not an obstacle for an offline experiment, but it could present issues for real-time imaging. Improvements to the total processing time are feasible.

Minimum bending energy curve fitting works well with a small number of samples compared to a least-squares curve fit using a large number of samples. Linear regression is inadequate. Lowish-order polynomial regression works decently if there are many measurements and if the needle isn't subject to multiple bends.

The bending energy minimization approach is not guaranteed to provide a feasible solution for every possible combination of constraints and sample points.

5.2 Future Work

An important follow-on will be to demonstrate real-time tracking using live MRI imaging. This will require implementation of a communication protocol that transmits scan plane poses to the MRI controller and listens for new image data. Precedent exists for controlling an MRI scanner in this way [9].

The time required to compute the needle curve optimization is very high and not currently suited for real-time operation. Reducing the number of numerical approxi-

mations in the optimization function would probably reduce the computational load, as would rewriting the needle modeling Python packages in C++.

5.3 Conclusion

This thesis presented a closed-loop model-based needle localization strategy agnostic to the imaging modality. A simulated multi-step needle insertion in MRI was tracked, and the error between the estimated position of the needle shaft from the model and the measured position of the centroid of the needle artifact was comparable to published needle localization approaches. The bending energy minimization approach produces accurate curve fits using a small number of images by also considering the kinematics of the insertion platform. While not extensively explored in this work, the parametric polynomial needle curve and the concept of planning scan planes using the curve could work for a very wide array of needle trajectories, including loops and other paths rarely explored in other literature.

References

- [1] J. Tokuda, K. Tuncali, I. Iordachita, S.-E. Song, A. Fedorov, S. Oguro, A. Lasso, F. M. Fennessy, C. M. Tempany, and N. Hata, “In-bore setup and Software for 3T MRI-guided Transperineal Prostate Biopsy,” *Physics in medicine and biology*, vol. 57, no. 18, pp. 5823–5840, Sep. 2012.
- [2] S. Misra, K. Reed, B. Schafer, K. Ramesh, and A. Okamura, “Mechanics of Flexible Needles Robotically Steered through Soft Tissue,” *The International Journal of Robotics Research*, vol. 29, no. 13, pp. 1640–1660, Nov. 2010.
- [3] R. J. Roesthuis, M. Abayazid, and S. Misra, “Mechanics-based model for predicting in-plane needle deflection with multiple bends,” in *2012 4th IEEE RAS EMBS International Conference on Biomedical Robotics and Biomechatronics (BioRob)*, Jun. 2012, pp. 69–74.
- [4] R. J. Webster, J. S. Kim, N. J. Cowan, G. S. Chirikjian, and A. M. Okamura, “Nonholonomic Modeling of Needle Steering,” *The International Journal of Robotics Research*, vol. 25, no. 5-6, pp. 509–525, May 2006.
- [5] O. Goksel, E. Dehghan, and S. E. Salcudean, “Modeling and simulation of flexible needles,” *Medical Engineering and Physics*, vol. 31, no. 9, pp. 1069–1078, Nov. 2009.
- [6] K. B. Reed, V. Kallem, R. Alterovitz, K. Goldbergxz, A. M. Okamura, and N. J. Cowan, “Integrated planning and image-guided control for planar needle steering,” in *2008 2nd IEEE RAS EMBS International Conference on Biomedical Robotics and Biomechatronics*, Oct. 2008, pp. 819–824.
- [7] R. J. Roesthuis, N. J. van de Berg, J. J. van den Dobbelen, and S. Misra, “Modeling and steering of a novel actuated-tip needle through a soft-tissue simu-

- lant using Fiber Bragg Grating sensors,” in *2015 IEEE International Conference on Robotics and Automation (ICRA)*, May 2015, pp. 2283–2289.
- [8] D. C. Rucker, B. A. Jones, and R. J. W. III, “A Geometrically Exact Model for Externally Loaded Concentric-Tube Continuum Robots,” *IEEE Transactions on Robotics*, vol. 26, no. 5, pp. 769–780, Oct. 2010.
 - [9] N. A. Patel, T. van Katwijk, G. Li, P. Moreira, W. Shang, S. Misra, and G. S. Fischer, “Closed-loop asymmetric-tip needle steering under continuous intraoperative MRI guidance,” in *2015 37th Annual International Conference of the IEEE Engineering in Medicine and Biology Society (EMBC)*, Aug. 2015, pp. 4869–4874.
 - [10] G. J. Vrooijink, M. Abayazid, S. Patil, R. Alterovitz, and S. Misra, “Needle path planning and steering in a three-dimensional non-static environment using two-dimensional ultrasound images,” *The International Journal of Robotics Research*, vol. 33, no. 10, pp. 1361–1374, Sep. 2014.
 - [11] G. Pernelle, A. Mehrtash, L. Barber, A. Damato, W. Wang, R. T. Seethamraju, E. Schmidt, R. Cormack, W. Wells, A. Viswanathan, and T. Kapur, “Validation of Catheter Segmentation for MR-guided Gynecologic Cancer Brachytherapy,” *Medical image computing and computer-assisted intervention : MICCAI ... International Conference on Medical Image Computing and Computer-Assisted Intervention*, vol. 16, no. 0 3, pp. 380–387, 2013.
 - [12] R. J. Roesthuis, M. Kemp, J. J. van den Dobbelaar, and S. Misra, “Three-Dimensional Needle Shape Reconstruction Using an Array of Fiber Bragg Grating Sensors,” *IEEE/ASME Transactions on Mechatronics*, vol. 19, no. 4, pp. 1115–1126, Aug. 2014.
 - [13] J. G. R. Bomers, J. P. M. Sedelaar, J. O. Barentsz, and J. J. Fütterer, “MRI-Guided Interventions for the Treatment of Prostate Cancer,” *American Journal of Roentgenology*, vol. 199, no. 4, pp. 714–720, Oct. 2012.
 - [14] S. Nath, Z. Chen, N. Yue, S. Trumppore, and R. Peschel, “Dosimetric effects of needle divergence in prostate seed implant using ^{125}I and ^{103}Pd radioactive seeds,” *Medical Physics*, vol. 27, no. 5, pp. 1058–1066, May 2000.

- [15] J. H. Youk, E.-K. Kim, M. J. Kim, J. Y. Lee, and K. K. Oh, “Missed breast cancers at US-guided core needle biopsy: How to reduce them,” *Radiographics: A Review Publication of the Radiological Society of North America, Inc*, vol. 27, no. 1, pp. 79–94, 2007 Jan-Feb.
- [16] G. Onik, E. R. Cosman, T. H. Wells, H. I. Goldberg, A. A. Moss, P. Costello, R. A. Kane, W. I. Hoddick, and B. Demas, “CT-guided aspirations for the body: Comparison of hand guidance with stereotaxis,” *Radiology*, vol. 166, no. 2, pp. 389–394, Feb. 1988.
- [17] C. R. Weiss, S. G. Nour, and J. S. Lewin, “MR-guided biopsy: A review of current techniques and applications,” *Journal of Magnetic Resonance Imaging*, vol. 27, no. 2, pp. 311–325, Feb. 2008.
- [18] A. V. D'amico, C. M. Tempany, R. Cormack, N. Hata, M. Jinzaki, K. Tunçali, M. Weinstein, and J. P. Richie, “TRANSPERINEAL MAGNETIC RESONANCE IMAGE GUIDED PROSTATE BIOPSY,” *The Journal of Urology*, vol. 164, no. 2, pp. 385–387, Aug. 2000.
- [19] “3D Slicer,” <https://www.slicer.org/>.
- [20] A. Fedorov, R. Beichel, J. Kalpathy-Cramer, J. Finet, J.-C. Fillion-Robin, S. Pu-jol, C. Bauer, D. Jennings, F. Fennessy, M. Sonka, J. Buatti, S. Aylward, J. V. Miller, S. Pieper, and R. Kikinis, “3D Slicer as an Image Computing Platform for the Quantitative Imaging Network,” *Magnetic resonance imaging*, vol. 30, no. 9, pp. 1323–1341, Nov. 2012.
- [21] J. S. Lewin, J. L. Duerk, V. R. Jain, C. A. Petersilge, C. P. Chao, and J. R. Haaga, “Needle localization in MR-guided biopsy and aspiration: Effects of field strength, sequence design, and magnetic field orientation.” *American Journal of Roentgenology*, vol. 166, no. 6, pp. 1337–1345, Jun. 1996.
- [22] S.-E. Song, N. B. Cho, I. Iordachita, P. Guion, G. Fichtinger, A. Kaushal, K. Camphausen, and L. L. Whitcomb, “Biopsy Needle Artifact Localization in MRI-guided Robotic Transrectal Prostate Intervention,” *IEEE transactions on bio-medical engineering*, vol. 59, no. 7, pp. 1902–1911, Jul. 2012.

- [23] N. J. Cowan, K. Goldberg, G. S. Chirikjian, G. Fichtinger, R. Alterovitz, K. B. Reed, V. Kalle, W. Park, S. Misra, and A. M. Okamura, “Robotic Needle Steering: Design, Modeling, Planning, and Image Guidance,” in *Surgical Robotics*. Springer, Boston, MA, 2011, pp. 557–582.
- [24] K. B. Reed, A. M. Okamura, and N. J. Cowan, “Modeling and Control of Needles With Torsional Friction,” *IEEE Transactions on Biomedical Engineering*, vol. 56, no. 12, pp. 2905–2916, Dec. 2009.
- [25] J. P. Swensen, M. Lin, A. M. Okamura, and N. J. Cowan, “Torsional Dynamics of Steerable Needles: Modeling and Fluoroscopic Guidance,” *IEEE Transactions on Biomedical Engineering*, vol. 61, no. 11, pp. 2707–2717, Nov. 2014.
- [26] A. Chentanez, C. Ritchie, G. Hauser, and O. Shewchuk, “Interactive Simulation of Surgical Needle Insertion and Steering,” p. 10, 2009.
- [27] E. Dehghan, O. Goksel, and S. E. Salcudean, “A Comparison of Needle Bending Models,” in *Medical Image Computing and Computer-Assisted Intervention – MICCAI 2006*, ser. Lecture Notes in Computer Science. Springer, Berlin, Heidelberg, Oct. 2006, pp. 305–312.
- [28] A. C. Barnett, Y.-S. Lee, and J. Z. Moore, “Fracture Mechanics Model of Needle Cutting Tissue,” *Journal of Manufacturing Science and Engineering*, vol. 138, no. 1, pp. 011 005–011 005–8, Sep. 2015.
- [29] M. Abayazid, R. J. Roesthuis, R. Reilink, and S. Misra, “Integrating Deflection Models and Image Feedback for Real-Time Flexible Needle Steering,” *IEEE Transactions on Robotics*, vol. 29, no. 2, pp. 542–553, Apr. 2013.
- [30] S. P. DiMaio and S. E. Salcudean, “Needle insertion modeling and simulation,” *IEEE Transactions on Robotics and Automation*, vol. 19, no. 5, pp. 864–875, Oct. 2003.
- [31] D. Glozman and M. Shoham, “Image-Guided Robotic Flexible Needle Steering,” *IEEE Transactions on Robotics*, vol. 23, no. 3, pp. 459–467, Jun. 2007.

- [32] P. J. Swaney, J. Burgner, H. B. Gilbert, and R. J. Webster, “A Flexure-Based Steerable Needle: High Curvature With Reduced Tissue Damage,” *IEEE Transactions on Biomedical Engineering*, vol. 60, no. 4, pp. 906–909, Apr. 2013.
- [33] R. J. Webster, J. M. Romano, and N. J. Cowan, “Mechanics of Precurved-Tube Continuum Robots,” *IEEE Transactions on Robotics*, vol. 25, no. 1, pp. 67–78, Feb. 2009.
- [34] P. E. Dupont, J. Lock, B. Itkowitz, and E. Butler, “Design and Control of Concentric-Tube Robots,” *IEEE transactions on robotics : a publication of the IEEE Robotics and Automation Society*, vol. 26, no. 2, pp. 209–225, Apr. 2010.
- [35] J. Carriere, C. Rossa, N. Usmani, R. Sloboda, and M. Tavakoli, “Needle shape estimation in soft tissue based on partial ultrasound image observation,” in *2015 IEEE International Conference on Robotics and Automation (ICRA)*, May 2015, pp. 2277–2282.
- [36] C. Rossa, M. Khadem, R. Sloboda, N. Usmani, and M. Tavakoli, “Adaptive Quasi-Static Modelling of Needle Deflection During Steering in Soft Tissue,” *IEEE Robotics and Automation Letters*, vol. 1, no. 2, pp. 916–923, Jul. 2016.
- [37] F. Zijlstra, J. G. Bouwman, I. Braškuté, M. A. Viergever, and P. R. Seevinck, “Fast Fourier-based simulation of off-resonance artifacts in steady-state gradient echo MRI applied to metal object localization,” *Magnetic Resonance in Medicine*, vol. 78, no. 5, pp. 2035–2041, Nov. 2017.
- [38] S. Patil, J. Burgner, R. J. Webster, and R. Alterovitz, “Needle Steering in 3-D Via Rapid Replanning,” *IEEE transactions on robotics : a publication of the IEEE Robotics and Automation Society*, vol. 30, no. 4, pp. 853–864, Aug. 2014.
- [39] W. Wang, C. L. Dumoulin, A. N. Viswanathan, Z. T. H. Tse, A. Mehrtash, W. Loew, I. Norton, J. Tokuda, R. T. Seethamraju, T. Kapur, A. L. Damato, R. A. Cormack, and E. J. Schmidt, “Real-time active MR-tracking of metallic stylets in MR-guided radiation therapy,” *Magnetic resonance in medicine : official journal of the Society of Magnetic Resonance in Medicine / Society of Magnetic Resonance in Medicine*, vol. 73, no. 5, pp. 1803–1811, May 2015.

- [40] D. Kraft, *A Software Package for Sequential Quadratic Programming.* Koln: DFVLR, 1988, open Library ID: OL18926873M.